J. Fluid Mech. (1987), *vol.* 175, *pp.* 247–293
Printed in Great Britain

Trailing vortices in the wakes of surface-mounted obstacles

By P. J. MASON
Meteorological Office, Bracknell, UK

AND B. R. MORTON
Department of Mathematics, Monash University, Melbourne, Australia

(Received 5 June 1985 and in revised form 14 July 1986)

The generation of trailing vortices in the wakes of surface-mounted obstacles at moderate Reynolds numbers is examined by channel-flow experiments and numerical simulation. A skew-mounted obstacle generates a single concentrated trailing vortex, together with weak streamwise vorticity of opposite sense extending to considerable distances on either side and zero gross circulation across the whole stream. Cross-stream-symmetrical obstacles (having a streamwise plane of symmetry normal to the plane surface) generate one or more nested vortex pairs, usually of alternate sense, of which one pair is normally dominant. The sense of rotation of the dominant vortex pair depends on both the shape of the obstacle and its depth relative to that of the boundary layer. Obstacles that divide the stream laterally produce dominant vortex pairs with a central downwash, whereas those lifting the flow predominantly over their crests produce dominant vortex pairs with a central upwash. It is argued that the vorticity of the dominant trailing vortices is generated largely as a component of cross-stream vorticity at the boundary, shed as a shear layer from the body, and turned inertially by the flow to form trailing vortices. It should also be emphasized that the dominant trailing vortex or vortex pair is generally embedded in a weak distribution of trailing vorticity of opposite signs, but with net circulation comparable with that of the dominant core.

1. Introduction

Two types of trailing-vortex wake behind surface-mounted obstacles have been identified in the literature: *horseshoe vortices* behind symmetrical obstacles, and *solitary trailing vortices* behind obstacles skew to the stream. Both are reasonably well known, although there has been some confusion of nomenclature. Trailing vortices of various senses prove to be a common feature of the wakes behind most obstacles but cannot entirely be explained in terms of these earlier models. Here we shall limit discussion to two classes of surface-mounted obstacle in flow over a horizontal plane. These comprise bodies with *cross-stream symmetry* having a vertical plane of symmetry parallel to the undisturbed stream and those with *skew symmetry* obtained by turning cross-stream-symmetrical bodies about a vertical axis.

Horseshoe vortices are supposed to be concentrated U-shaped vortices that form wherever boundary-layer vorticity is advected round a surface-mounted obstacle. Approaching vorticity is believed to pile up ahead of the obstacle and be stretched away downstream in two arms which form a trailing-vortex pair. The sense of circulation is downwards towards the boundary in front of the obstacle, with the

trailing vortices combining to produce downwash in the centre of the wake behind the obstacle. Aerodynamicists believe that horseshoe vortices of this kind form around struts at their junctions with wings and around wings where they join aircraft bodies. The mechanism has also been used to account for trailing vortices observed in boundary layers behind surface protuberances (Sedney 1973), for vortices around buildings (Hunt 1971) and for vortex wakes behind hills (Hunt & Snyder 1980).

Flow upstream of surface mounted obstacles has been studied in a number of cases (e.g. Gregory & Walker 1951; Morkovin 1972; Baker 1979, 1980) and depends on the Reynolds number. At low Reynolds numbers the boundary-layer flow is free from organized vortices upstream of the body. At moderate Reynolds numbers the approaching flow separates from the lower boundary and there is a simple vortex of 'horseshoe sense', its circulation growing with increasing Reynolds number. An increasingly complex structure of vortices then develops, in which further pairs of counter-rotating vortices appear at progressively higher Reynolds numbers until the boundary layer becomes turbulent. Even in fully developed turbulent boundary layers, however, a mean vortex structure survives (Baker 1980). It should be noted that the conceptual model for horseshoe vortices only accounts for one sign of vorticity and cannot directly encompass such counter-rotating vortices. To explain the counter-rotating vortices account must be taken of the generation of vorticity at the lower boundary and over the surface of the body.

Detailed observations of the wakes of bodies generating so-called horseshoe vortices have also shown the existence of more than one trailing-vortex pair, (e.g. Gregory & Walker 1956; Mochizuki 1961; Hunt & Snyder 1980). In most cases the wakes contain nested pairs of vortices with alternate sense of rotation. Although it has been suggested that the dominant trailing-vortex pair represents the trailing arms of the horseshoe vortex, careful observation suggests that only the outermost vortices relate directly to those upstream. The inner (and perhaps stronger) vortices appear to be a product of the inner wake and are observed only downstream of the obstacle. For moderate Reynolds numbers, at least, those inner vortices are dominant and may exhibit either a central upwash or a central downwash according to the nature of the obstacle. At larger Reynolds numbers, when either the wake or both the boundary layer and wake are turbulent, it is more difficult to determine the structure of wake vortices, but there is evidence of the presence of trailing vortices which survive far downstream in the mean flow; the relatively few documented cases appear to show central downwash (Hansen 1975). An examination of these flows at high Reynolds numbers is beyond the scope of the present study.

Single trailing vortices behind slant (vortex-generator) plates have been used in modifying aerodynamic boundary layers and have been observed in topographic flows downwind of Gibraltar (Cook, Coulson & McKay 1978) and the island of Ailsa Craig (Jenkins *et al.* 1981). These vortices again appear to be a product of the wake and not a residue of upstream circulation. They have been identified as lateral 'lifting' vortices associated with surface-mounted obstacles skew to the wind, and representing (supposedly with their mirror images in the plane boundary of both obstacle and trailing vortex) effective trailing-vortex pairs behind lifting aerodynamic bodies. In fact this represents an over-simplification as the no-slip condition is inconsistent with the image system, and we shall see that vorticity generated at the lower boundary plays an important role.

The effects of organized streamwise vorticity in wakes may be of considerable importance: for example, it modifies the wake structure so as to significantly increase the lateral transport of longitudinal momentum between the outer stream and

boundary, and it may be responsible for a large increase in drag behind obstacles in boundary layers. In view of the interest and importance of wake vortices, it is clear from this limited review of earlier work that the processes giving rise to wake circulation in flow past surface-mounted obstacles are inadequately understood. Our own study began from two points of reference. One was to understand the connectivity of the vorticity field when a skew surface-mounted obstacle generates a solitary trailing vortex; the other was to explain the dominant trailing-vortex pair with central upwash obtained in a numerical simulation of flow over a symmetrical rounded obstacle. All the examples we discuss below are for steady flow at no more than moderate Reynolds numbers. This limitation makes it a good deal easier to interpret both the laboratory and numerical simulations, but we must emphasize that our results do not necessarily carry over to the mean fields in turbulent flows, although they should give some guidance.

Flow past bluff bodies is highly nonlinear and three-dimensional and there is little prospect of obtaining analytic solutions. It is natural, therefore, that we should use numerical simulation and laboratory experiments to gain insight. In the following account §2 presents some basic ideas as a framework for the subsequent discussion; §3 describes the results from the numerical integration of the Navier–Stokes equations for flow over smoothly rounded hills; §4 describes results for flow past various bodies in a water channel; and §5 summarizes the main results and conclusions.

2. General considerations

A number of rather general results are available on the generation of vorticity at boundaries, its advection and reorientation in the flow, and on the possible distribution of streamwise vorticity including trailing vortices behind obstacles. We shall show that diffusive annihilation of boundary-layer vorticity by vorticity of opposite sense generated at the boundary is of central importance in the description of flow over obstacles. We begin, however, by treating surface generation and inertial turning of vorticity within the fluid separately.

2.1. *The generation of vorticity*

Existing vorticity can be processed in the interior of homogeneous fluids by stretching and turning, but there is no mechanism whatsoever for the generation of fresh vorticity within the flow. It is, indeed, well known that all new generation of vorticity in homogeneous fluids must take place at the boundaries. Lighthill (1963) has shown that the normal flux of tangential vorticity at a plane boundary with unit normal $\boldsymbol{n}$ is

$$-\frac{1}{\rho}(\boldsymbol{n}\times\nabla)p, \tag{1}$$

where p is the dynamic pressure, while Morton (1984) has argued that the total rate of generation of tangential vorticity per unit surface area of a fixed rigid boundary is

$$-\frac{1}{\rho}(\boldsymbol{n}\times\nabla)p-\frac{\mathrm{d}}{\mathrm{d}t}(\boldsymbol{n}\times U_{\mathrm{B}}), \tag{2}$$

where U_{B} is the tangential velocity of the boundary. For flow past fixed obstacles, the entire surface is stationary and the sole means of generation of vorticity is by tangential pressure gradients along the boundary.

The velocity in a boundary layer increases from zero at the wall to the full-stream value at its outer edge with a corresponding increase in total head ($H = \frac{1}{2}\rho u^2 + p_t$, where u is the fluid velocity and p_t is the total fluid pressure). Because of friction, this total head is not conserved, but in many cases the rate of viscous dissipation is relatively small and may be neglected over short distances. The primary effect of any obstacle is always to divert flow, and this it does by creating a disturbance pressure field which slows down fluid in direct approach to the body and accelerates it laterally either over or round the body. Thus all obstacles generate local pressure maxima on their upstream faces. As the flow is accelerated over the crest and around the sides of the obstacle the approximate local invariance of head implies a local pressure reduction. In accordance with (1), vortex filaments are created continuously in closed loops which coincide with isobars and have anticlockwise sense about a pressure maximum and clockwise sense about a pressure minimum (a surface pressure field generated by a numerical model is illustrated in figure 4 and discussed below). Vorticity generated at the surface is carried out into the flow by diffusion and is then subject, with the boundary-layer vorticity, to inertial turning and stretching. All vorticity generated upstream of the surface pressure maximum has a (cross-flow) component opposite in sense to that of the vorticity imported in the boundary layer and will suffer at least partial annihilation by cross-diffusion. Over the crest of the obstacle there is strong generation of vorticity having a component with like sense to that in the upstream boundary layer. We are concerned particularly with obstacles producing lee separation of flow, and the strong thin shear layer generated over the crest and flanks of the obstacle and advected into the wake downstream of separation then plays a dominant role.

The pressure field generated by a skew object and the vorticity generated at its surface exhibit broadly the same features except that there is no longer cross-stream symmetry. An example of such a pressure field from the numerical simulation is shown in figure 20.

It should be noted that the gross rate of generation of vorticity between two stations A and B is proportional to the net pressure difference $p_A - p_B$. The computational domain in our numerical study was $10L$ in width, where L is the radius at the base of the obstacle. There is no pressure difference across the domain for symmetrical obstacles but there is for skew obstacles, and in the latter case there is a small progressive net generation of streamwise vorticity at the boundaries as we move through the working section.

2.2. *Production of streamwise vorticity by turning boundary-layer vorticity round an obstacle*

In this section we concentrate attention on the turning (or tilting as it is sometimes called) of boundary-layer vorticity advected round an obstacle and for the moment neglect both the generation of fresh vorticity and effects of diffusion. Far upstream, the boundary layer may be represented as a distribution of vortex filaments which are parallel to the boundary and normal to the main stream. There is a decrease in the local advection velocity ahead of the body, an increase to the sides, and no change at large lateral distances. Thus the main deformation of a vortex filament advected in the upper boundary layer around the obstacle is retardation upstream of the obstacle, turning towards the obstacle on either side, and advection without change far to either side.

One important property of filaments of boundary-layer vorticity as they are advected towards and locally turned about an obstacle is their connectivity. If

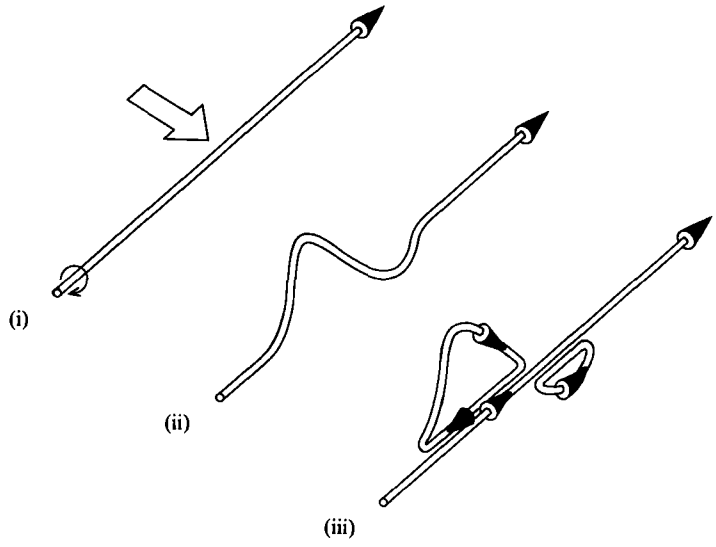

FIGURE 1. Advected filaments of boundary-layer vorticity (i) are distorted by an obstacle (ii) and the distorted form is equivalent to the initial straight filament together with a set of closed vortex loops (iii).

diffusion is neglected, a vortex filament can be locally distorted by a combination of turning, and stretching but this will not affect its local strength (measured by the vorticity intersecting a cross-section); moreover, it is possible to sever the filament. A locally distorted filament, as illustrated in figure 1, is entirely equivalent to an undisturbed filament together with one or more closed loops of equal strength. It follows that the reorientation of vorticity around the obstacle can produce local changes of circulation in circuits normal to the undisturbed stream, but it cannot produce global changes in normal circuits which enclose the *whole* flow disturbance due to the obstacle. The only effects of reintroducing viscosity will be an exchange of vorticity between adjacent filaments and, where these are of opposite sense, mutual annihilation of the two senses of vorticity and reconnection of the filaments. Thus, the effect of diffusion on configuration (iii) of figure 1 would be to recreate configuration (ii).

2.3. *Global circulation*

Consider a uniform stream U flowing in the x-direction over a plane boundary $z = 0$ past an obstacle of arbitrary shape mounted on the lower boundary in a neighbourhood of the coordinate origin (figure 2). In the undisturbed approaching boundary layer all vorticity is in the y-direction, but vorticity with a streamwise component is produced (i) by turning of incident boundary-layer vorticity, and (ii) by generation of vorticity at the boundary and surface of the obstacle in the disturbance pressure field. The circulation in the circuit $\mathscr{C}(0)$ in the plane $x = 0$, corresponding with

$$0, \quad B \to (0, \infty, 0), \quad C \to (0, \infty, \infty), \quad E \to (0, -\infty, -\infty), \quad A \to (0, -\infty, 0), \quad 0,$$

but following the curve of intersection of obstacle surface and plane near 0, is

$$k(y_A, y_B) \to k(-\infty, \infty) = \int_{\mathscr{C}(0)} \boldsymbol{v} \cdot \mathrm{d}\mathbf{r} = \int_{x=0} \xi \, \mathrm{d}y \, \mathrm{d}z = 0,$$

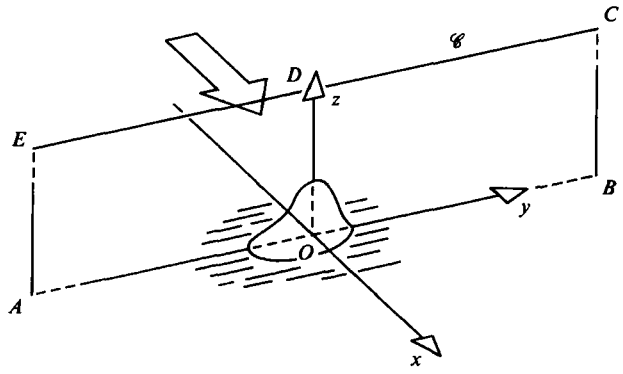

FIGURE 2. Coordinate system for flow past an arbitrary obstacle.

since $v = 0$ everywhere on the boundary $z = 0$ and obstacle surface, and since the stream is undisturbed far from the obstacle. (An estimate for the disturbance velocity at large distance, $R = (y^2+z^2)^{\frac{1}{2}}$, is provided by the disturbance due to an obstacle in an inviscid stream, with leading term of doublet character having distant velocity $O(R^{-2})$ contributing $O(R^{-1})$ to the circulation.) By the same argument,

$$\int_{\mathscr{C}(x)} \boldsymbol{\omega}\cdot\mathrm{d}\boldsymbol{A} = \int_x \xi\,\mathrm{d}y\,\mathrm{d}z = 0$$

for corresponding circuits $\mathscr{C}(x)$ in each and every plane $x =$ constant, where $|\mathrm{d}\boldsymbol{A}| = \mathrm{d}y\,\mathrm{d}y$ is the element of area in a cross-sectional plane. Streamwise circulation can be produced *locally* but not *globally* by turning advected boundary-layer vorticity (§2.2). Further, the total rate of generation of x-vorticity at the lower boundary in a strip of unit x-width is

$$\int_{-\infty}^{\infty} \frac{1}{\rho}\frac{\partial p}{\partial y}\,\mathrm{d}y = \left[\frac{1}{\rho}p\right]_{-\infty}^{\infty} = \frac{1}{\rho}(p_\infty - p_{-\infty}) = 0,$$

since the pressure disturbance at infinity is also zero. Thus, regardless of the shape and orientation of an obstacle, it is impossible to generate net streamwise circulation in the whole flow past a surface-mounted obstacle. This simple result, that the total circulation (or net streamwise vorticity) in cross-sectional circuits is zero for all x, has important implications. For example, there is ample evidence (Cook *et al.* 1978, for Gibraltar; Jenkins *et al.* 1981, for Ailsa Craig) that hills, ridges and islands skew to the wind may produce apparent solitary vortex wakes, and these have surprised observers with their strength. It is clear that these single dominant trailing vortices have significant circulation measured in circuits closely embracing the vortex core, but it follows also from the arguments above that these cores must be embedded in distributions of streamwise vorticity of opposite sense to yield zero total cross-stream circulation. The other streamwise vorticity must be relatively diffuse as it has not been reported. It should be particularly noted that earlier suggestions that the skew islands with single trailing vortex might be regarded as a half-span aerofoil extending above the boundary with image aerofoil and image trailing vortex below the boundary, equivalent in total to a finite lifting aerofoil with a vortex pair, are erroneous. Images have no place in viscous flows, and the streamwise vorticity which in an inviscid flow would be concentrated in an image vortex must in our flows be distributed through the flow.

2.4. *Circulation to one side of the obstacle*

In general there is vertical flow in the wake behind an obstacle, and according to the nature of the obstacle and its height relative to the incident boundary layer this may be upward (upwash) or downward (downwash). Hence there is non-zero circulation, $K(0, \infty)$, arising from the segment DO of the circuit,

$$0, \quad B \rightarrow (0, \infty, 0), \quad C \rightarrow (0, \infty, \infty), \quad D(0, 0, \infty), \quad 0,$$

but following the curve of intersection of the obstacle surface and plane near O, and also in parallel circuits ($x =$ constant) from some distance upstream to far downstream of the body. For cross-stream-symmetric bodies both turning of the advected vorticity and generation of vorticity at the boundary by pressure gradients are antisymmetric about the symmetry plane, and it follows that streamwise vorticity in the wakes of symmetric obstacles must be organized into a vortex pair or a multiple system of vortex pairs, usually with a single dominant pair. We shall find that the core circulation of the dominant vortex may be almost an order of magnitude greater than the one-sided circulation.

2.5. *A synthesis of the generation, processing and diffusion of vorticity*

We complete this section with a brief synthesis of the effects of generation, diffusion and inertial processing (turning and stretching) of vorticity for the case of the traditional horseshoe vortex. The presence of flow separation at the baseplate upstream of the obstacle with reattachment on the upstream face of the obstacle implies downflow over the lower part of the face with upflow over the crest. The two levels of flow must therefore be separated by at least one dividing streamline, terminating on the upstream face at an attachment point. According to the traditional conceptual model of horseshoe vortices, boundary-layer vorticity ($\eta = \partial u/\partial z$) advected towards the obstacle below this streamline is trapped upstream and turned and stretched to either side of the obstacle, thereby producing a concentrated vortex wrapped around the obstacle with arms trailing downstream.

The traditional model neglects all generation of vorticity at boundaries, but it is not difficult to assess the importance of vorticity generation, at least when the upstream boundary-layer depth is small relative to the height of the obstacle. For an obstacle with cross-stream symmetry, we may then assume that the dynamic pressure at the separation point on the leading edge is $\frac{1}{2}\rho U^2$, and it follows by integration of (1) along the upstream boundary and up the leading edge of the obstacle to the separation point that the gross rate of generation of vorticity over this region of boundary is $-\frac{1}{2}U^2$. This is precisely equal and opposite to the rate at which vorticity is advected in the boundary layer towards the obstacle.

$$\int u\eta \, \mathrm{d}z = \tfrac{1}{2}U^2.$$

There is, therefore, a balance between advective import and production of vorticity in the upstream plane of symmetry, and the circulation per unit streamwise length taken through the full depth of the boundary layer must decrease to zero as the obstacle is approached. Within the decreasing circulation there will generally remain a residue of positive vorticity in the upper boundary layer and negative vorticity near the boundary at which it has been generated. Except at low Reynolds numbers, diffusion by itself acts too slowly to intermix these separate concentrations as the obstacle is approached. The nested structure of vortices observed upstream of

obstacles at moderate Reynolds numbers, each geometrically similar to a horseshoe vortex but with sense of rotation that alternates with increasing distance from the obstacle, presumably serves to sharpen vorticity gradients and so enhance cross-diffusion. These multiple vortices extend round the sides of obstacles, although at moderate Reynolds numbers they decay fairly rapidly by cross-diffusion and may not extend past the obstacle. Only the generation of vorticity of opposite sign and not just a flow instability can account for circulations with opposite vorticity.

The strong trailing vortices that have been observed in the centre of the wakes of obstacles (e.g. Gregory & Walker 1956) appear to be distinct from those seen at the sides and traceable to disturbances upstream of the obstacle. Our numerical and experimental results show that such wake vortices can be formed by the turning of vorticity which is generated over the surface of the obstacle and separates as a concentrated shear layer behind the crest or sides. The sense of turning and hence the sense of the organized vortex pair behind a symmetric obstacle depends on the shape of the obstacle and its height relative to that of the boundary layer. The solitary dominant vortices observed behind skew obstacles are also formed from vorticity generated at the surface of the obstacle and processed in the wake.

Although the results we shall describe are restricted to moderate Reynolds numbers, the underlying mechanism is at once so natural and so powerful that it seems likely that it should be relevant to the mean flow in turbulent wakes.

3. Numerical simulation of flow past surface-mounted obstacles

The numerical study was carried out to examine features of laminar flow past rounded obstacles using the Navier–Stokes equations for incompressible flow of a fluid with constant viscosity,

$$\frac{\partial \boldsymbol{v}}{\partial t} + \boldsymbol{v}\cdot\boldsymbol{\nabla}\boldsymbol{v} = -\boldsymbol{\nabla}p + \nu\boldsymbol{\nabla}^2\boldsymbol{v},$$

$$\boldsymbol{\nabla}\boldsymbol{v} = 0.$$

The numerical model is that described by Mason & Sykes (1979*a*) employing a Cartesian mesh and relying on the choice of flow parameters to ensure effective second-order accuracy. The consequent restrictions on flow parameters are significant but no more severe than the inevitable requirement that the computational mesh should resolve the shear layer shed from the obstacle. The corresponding maximum attainable Reynolds number of flow past the obstacle, with the computing resources available, was a few hundred. The model uses a well-established (Piacsek & Williams 1970) energy-conserving convective scheme and if applied outside its range of good approximation to a continuous solution will develop a 'rough' solution. Tests against analytic theory and laboratory experiments can be found in Mason & Sykes (1979*b*) and (1981) respectively. The coordinate system and boundary geometry are sketched in figure 3.

To avoid introducing flow on scales that the model and its mesh cannot resolve the obstacle must have a smooth shape. The first obstacle has shape,

$$z = s(x,y) = \begin{cases} h\cos^2[\pi(x_s^2+y_s^2)^{\frac{1}{2}}/2L], & x_s^2+y_s^2 < L, \\ 0, & x_s^2+y_s^2 \geqslant L, \end{cases}$$

where

$$x_s = b(x\cos\theta - y\sin\theta), \quad y_s = b^{-1}(y\cos\theta + x\sin\theta).$$

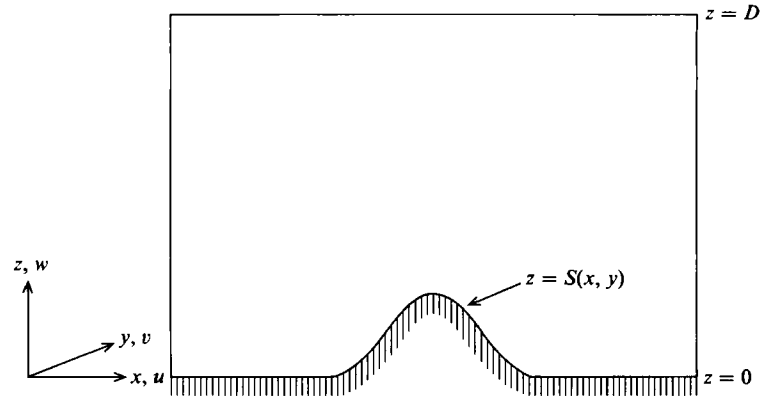

FIGURE 3. Schematic diagram in mid-plane ($y = 0$) of the domain of integration.

Parameter	Case A	Case B	Case C
Hill-base radius L/L	1	1	1
Hill height h/L	0.66	0.66	2.0
Uh/ν	100	300	150
$\bar{u}h/\nu$	30	120	108
$\bar{u}/U$	0.3	0.4	0.7
Domain length/L	20	20	26
Domain width/L	10	10	13
Domain height/L	10	10	13
Displacement thickness at centre of domain/L	0.55	0.40	0.55
Effective distance of centre of domain from start of Blasius flow/L	16	27	14

Case D has a hill of elliptical section with parameters otherwise as for case B.

TABLE 1. Parameters for the numerical simulations. All lengths are scaled in terms of the radius of the circular hill L; U is the free-stream velocity above the boundary layer and $\bar{u}$ is the mean velocity that would exist through the height interval $0 \leqslant z \leqslant h$ in the absence of the obstacle

Three cases with this type of obstacle were considered: A and B for circular hills with $b = 1$ and $\theta = 0$; and D for an elliptical hill with $b = \sqrt{2}$ and $\theta = \frac{1}{4}\pi$. The basic parameters and domain sizes for cases A and B are given in table 1; those for case D are the same as for case B. The second obstacle, case C, consisted of a cylinder surmounted with a hemisphere:

$$z = s(x, y) = \begin{cases} h(0.5 + 0.5(1 - (x^2+y^2)/L^2)^{\frac{1}{2}}), & x^2+y^2 < L, \\ 0, & x^2+y^2 \geqslant L. \end{cases}$$

In cases A, B and D the three-dimensional domain comprised a block of $42 \times 30 \times 30$ x, y, z gridpoints non-uniformly spaced with resolution varying from $\frac{1}{6}L$ near the obstacle to L near the upstream and downstream boundaries, where L is the radius of the base of the circular hill. In case C the obstacle is more bluff and a finer resolution is needed to meet the requirements of effective second-order accuracy. The domain comprises a block of $90 \times 60 \times 40$ x, y, z gridpoints non-

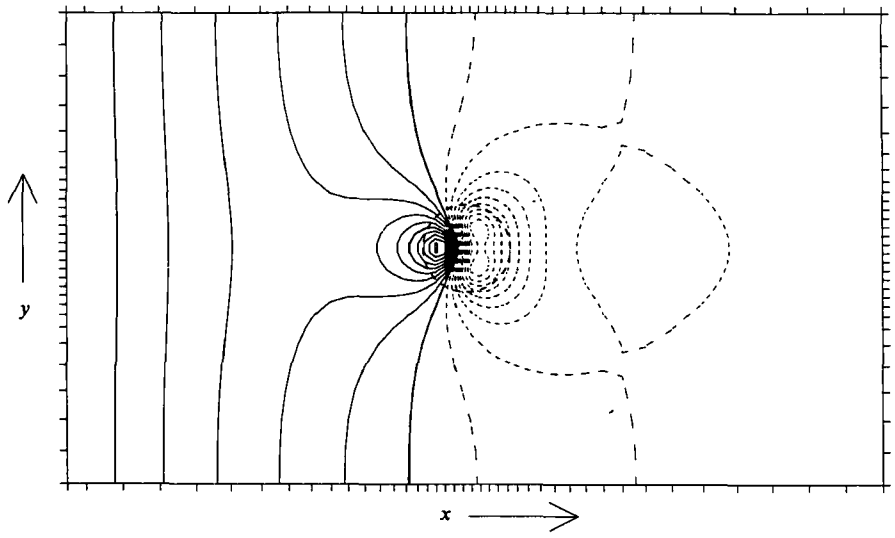

FIGURE 4. Surface pressure field for case A. The contours are projected vertically onto a horizontal plane. The zero of the pressure field has been determined by setting the horizontally averaged pressure at the top of the domain to zero. Negative values are denoted by dashed contours and contour interval is $0.0054U^2$, one tenth of the maximum value.

uniformly spaced with resolution varying from $\frac{1}{12}L$ near the obstacle to L near the upstream and downstream boundaries.

The boundary conditions used were: no-slip on the lower boundary and hill; rigid stress-free upper and lateral side boundaries; a specified Blasius boundary layer beneath a uniform stream U on the upstream boundary; and a simple outflow condition of zero second streamwise derivative on the downstream boundary to allow the Blasius layer to thicken and interact with the hill before exiting. The domain length is about $20L$, and its width and height about $10L$. The original selection of lateral boundary separation was intended to produce a negligible influence on the flow, but even at this distance there is a small pressure disturbance at the lateral boundaries.

3.1. *Vortex wakes of axisymmetric obstacles*

Two cases of flow past the smooth axisymmetric obstacle are examined, for two values of Reynolds number. Since the boundary layer is deep we define a relevant Reynolds number $\bar{u}h/\nu$, where

$$\bar{u} = \frac{1}{h}\int_0^h U(z)\,\mathrm{d}z,$$

where $U(z)$ is the undisturbed velocity profile that would exist at the obstacle location in the absence of the obstacle. Case A is for Reynolds number 30 and case B for 120; other parameters are given in table 1. The solutions obtained for these values of Reynolds number depend qualitatively on the exact value of the Reynolds number. The examples shown here have been selected to illustrate the behaviour at low and moderate values. A single case of flow past the more bluff obstacle at a Reynolds number $\bar{u}h/\nu$ of 108 is considered in case C (other parameters are given in table 1).

Solution fields for case A are presented in figures 4–7. Figure 4 represents the projection on to a horizontal plane of the surface pressure field on $z = s(x, y)$. The approaching flow is retarded ahead of the obstacle, with pressure on the surface rising

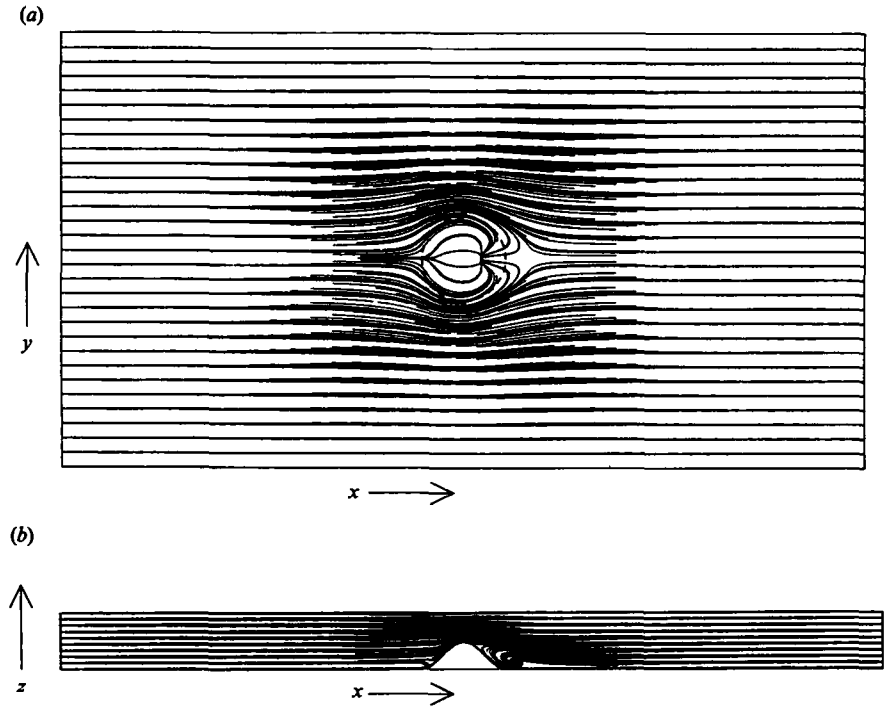

FIGURE 5. Flow directions for case A: (*a*) surface stress pattern, and (*b*) streamwise section in the centreplane. For economy only the part of the flow below $z = 2h$ is illustrated.

to a maximum at the forward stagnation point. Fluid is then accelerated round and especially over the crest of the obstacle with a broader region of reduced pressure downstream. The generation of vorticity at the boundary will be in accord with the discussion in §2.1. The weak mean pressure gradient across the domain is inconsistent with Blasius flow and is due to the finite depth of the computational domain.

Figure 5(*a*) shows trajectories in the surface stress field (see Mason & Sykes 1979*a* for computational details) and figure 5(*b*) shows flow trajectories in the vertical centreplane. There is rear separation, and in the vertical section a spiral node with sinking motion in the lee of the obstacle. Figure 6 shows transverse sections of the flow field in the vertical plane through the upstream edge of the hill and normal to the incident stream. Figure 7 shows such sections in the parallel plane through the downstream edge of the hill. The upstream sections include: (*a*) the streamwise component of velocity, (*b*) the transverse velocity field and (*c*) the streamwise component of vorticity $\xi = [(\partial u/\partial y) - (\partial v/\partial z)]$. The disturbance in the streamwise component of velocity is small in the upstream section, although it extends laterally and vertically to considerable distances, an indication that the pressure perturbation field is also extensive. As expected the upstream transverse velocity component is everywhere upward and outward as the flow is diverted round the obstacle. The uniform vertical flow associated with the thickening of the Blasius boundary layer may also be noted, especially in the upper parts of the section. The streamwise vorticity field at the upstream edge of the obstacle (figure 6*c*) has a quadrupole structure with a relatively weak upper vortex pair in the sense for central downwash. This upper pair can be traced to the turning of transverse boundary-layer vorticity. The stronger underlying pair associated with central upwash comprises vorticity that

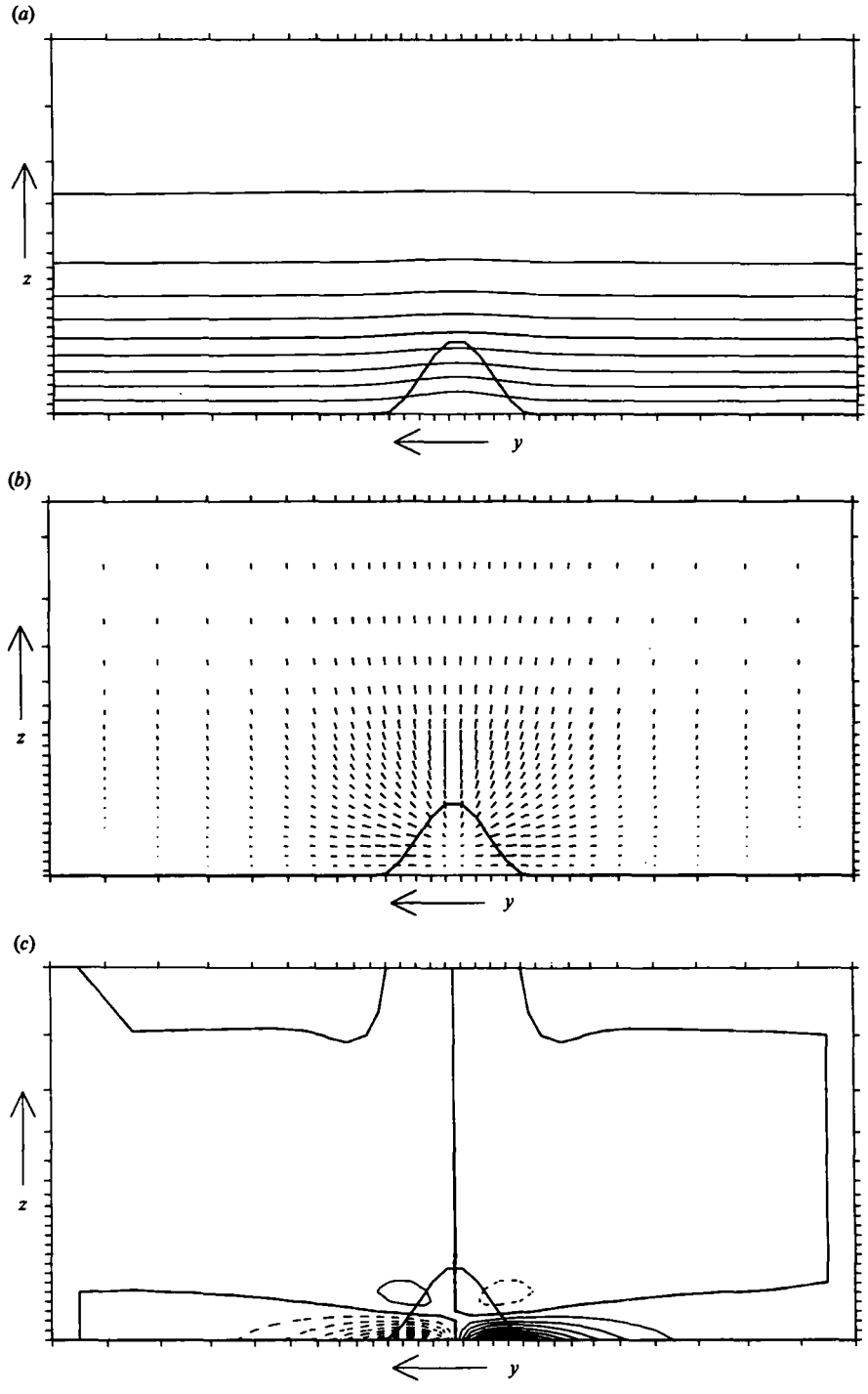

FIGURE 6. Transverse sections at the upstream extremity of the obstacle for case A showing: (*a*) contours of the streamwise velocity component with contour interval $0.1U$; (*b*) flow vectors showing transverse velocities. The maximum vertical velocity component has a magnitude $0.024U$; (*c*) Contours of the longitudinal vorticity ξ with contour interval $0.040U/L$, one tenth of the maximum value, and negative values denoted by dashed contours. An outline of the obstacle is given in each figure.

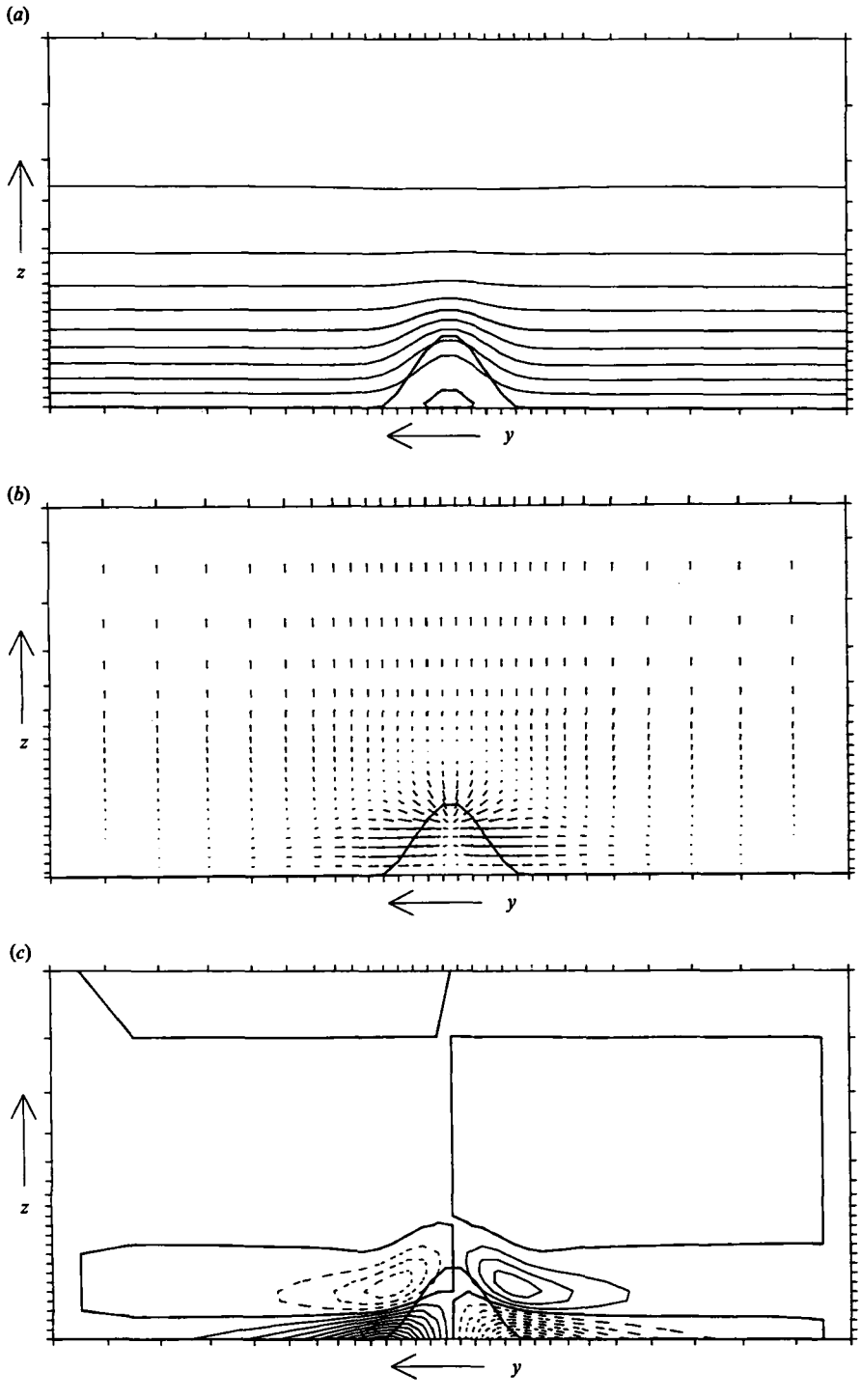

FIGURE 7. Transverse sections at the downstream extremity of the obstacle for case A. As figure 6. (*a*) U with contour interval $0.1U$ (note that the zero contour leaves the surface where the flow reverses); (*b*) transverse flow vectors with maximum vertical velocity magnitude $0.012U$, and (*c*) ξ with contour interval $0.029U/L$, one tenth of the maximum value. An outline of the obstacle is given in each figure.

has been generated at the boundary by the tangential component of the pressure gradient as it drives flow to the sides of the obstacle. This freshly generated vorticity has diffused out from the boundary, has suffered partial annihilation by cross-diffusion into the surviving boundary-layer vorticity overhead, and is itself being advected and turned with flow round the obstacle. Although the upper vortex pair has much weaker core vorticity than the freshly generated pair below, this is because the upper pair is older and much more diffuse than the recent pair below. The one-sided circulation associated with the region of the upper vortex is very similar in magnitude to that of the lower vortex with the result that the net circulation in the quadrant defined by positive y- and z-axes is small relative to each contribution separately, but with the upwash sense of the lower pair.

The flow field changes rapidly over the obstacle as the disturbance pressure field diverts the flow and generates vorticity at the boundary, and advection and diffusion modify the existing and newly generated vorticity. The downstream sections in a transverse plane through the rear edge of the hill are shown in figure 7. The streamwise perturbation behind the obstacle is substantially greater than upstream and represents the retarded flow of the wake. The transverse flow is broadly inward and downward, but with a rather more complex structure than in the upstream section. Although there is relatively strong downwash in the upper wake, there is weak upwash through an appreciable proportion of the height of the obstacle. This pattern may be better understood from the distribution of longitudinal vorticity in the section behind the obstacle (figure 7*c*), where there is again a quadrupole structure, but of opposite sense to that upstream. The lower vortex pair has downwash sense and relatively closely spaced contours which are open to the boundary, showing both that this is the most recently generated vorticity and that generation is proceeding actively in the disturbance pressure field as it turns the flow round the obstacle into the wake. The upper vortex pair is more diffuse and can be traced to the vorticity generated by pressure gradients upstream of the obstacle and subsequently diffused upwards and advected round it. Part of the vorticity generated upstream has been annihilated by cross-diffusion with the more recent vorticity of the lower pair, and part with the residual vorticity from the original boundary layer (which survives only in a very weak downwash vortex above both pairs shown and too weak to appear in the contour interval adopted). The two trailing-vortex pairs are of comparable strength, with the result that little evidence of circulation is shown in the transverse flow field of figure 7 (*b*). The distribution of streamwise vorticity behind the body may be regarded as comprising a lower level of rather concentrated vorticity generated on the flanks of the obstacle, a more diffuse middle level of vorticity of opposite sign generated on the approaches to the body, and a very diffuse upper level of vorticity of the same sign as the lower level which consists of incident boundary-layer vorticity turned around the obstacle. The three levels form a sloping stack which is in some ways analogous to the layered vorticity of decreasing strength above a plate oscillating steadily in its plane. At this location the net circulation in the quadrant defined by the postive y- and z-axes is weak and of the downwash sense; there is an approximate balance between the component vortex pairs. With increasing distance downstream the quadrupole of figure 7 (*c*) suffers continuing cross-diffusion and evolves into a very weak simple trailing-vortex pair with downwash.

Examination of flows at Reynolds numbers below that of case A shows that the structure of the longitudinal vorticity fields remains qualitatively similar, and enhanced diffusion prevents the generation of significant regions of concentrated vorticity.

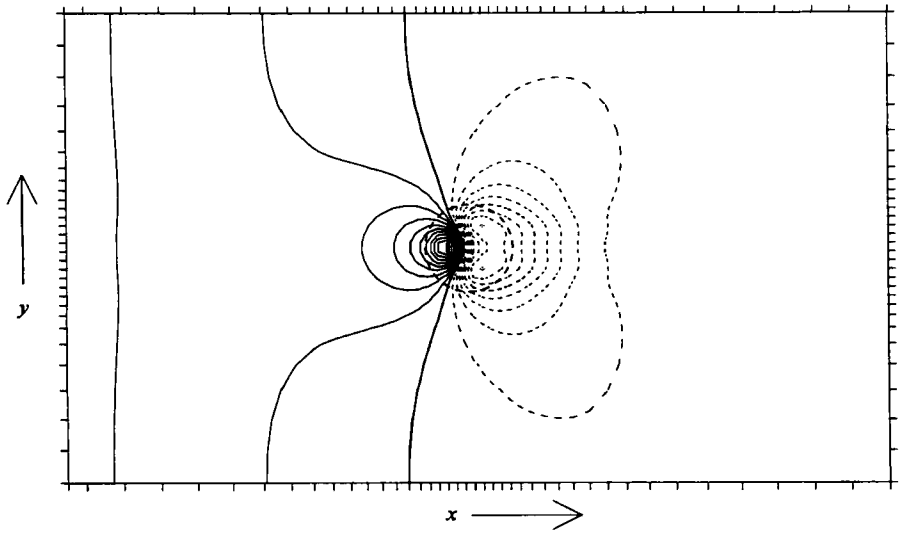

FIGURE 8. Surface pressure field for case B. Contour interval is $0.0059U^2$. See figure 4 for plotting convention.

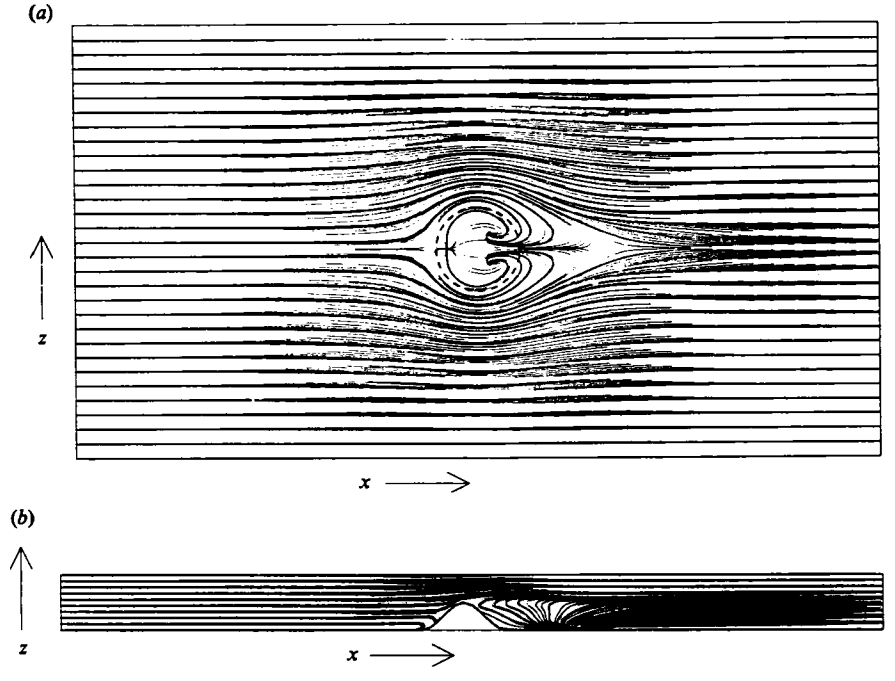

FIGURE 9. Flow directions for case B: (*a*) surface stress pattern and (*b*) streamwise section in the centreplane. For economy only the part of the flow below $z = 2h$ is illustrated.

Figures 8–12 show solution fields for case B at the higher Reynolds number of 120. This is smaller than the Reynolds number at which the flow becomes unsteady (about 160) but sufficiently far above that of case A to provide a significant reduction in diffusive effects. The surface pressure (figure 8) shows the same features as those seen in the lower-Reynolds-number case. The main differences from the lower-Reynolds-number case are a more extensive pressure minimum corresponding to a more

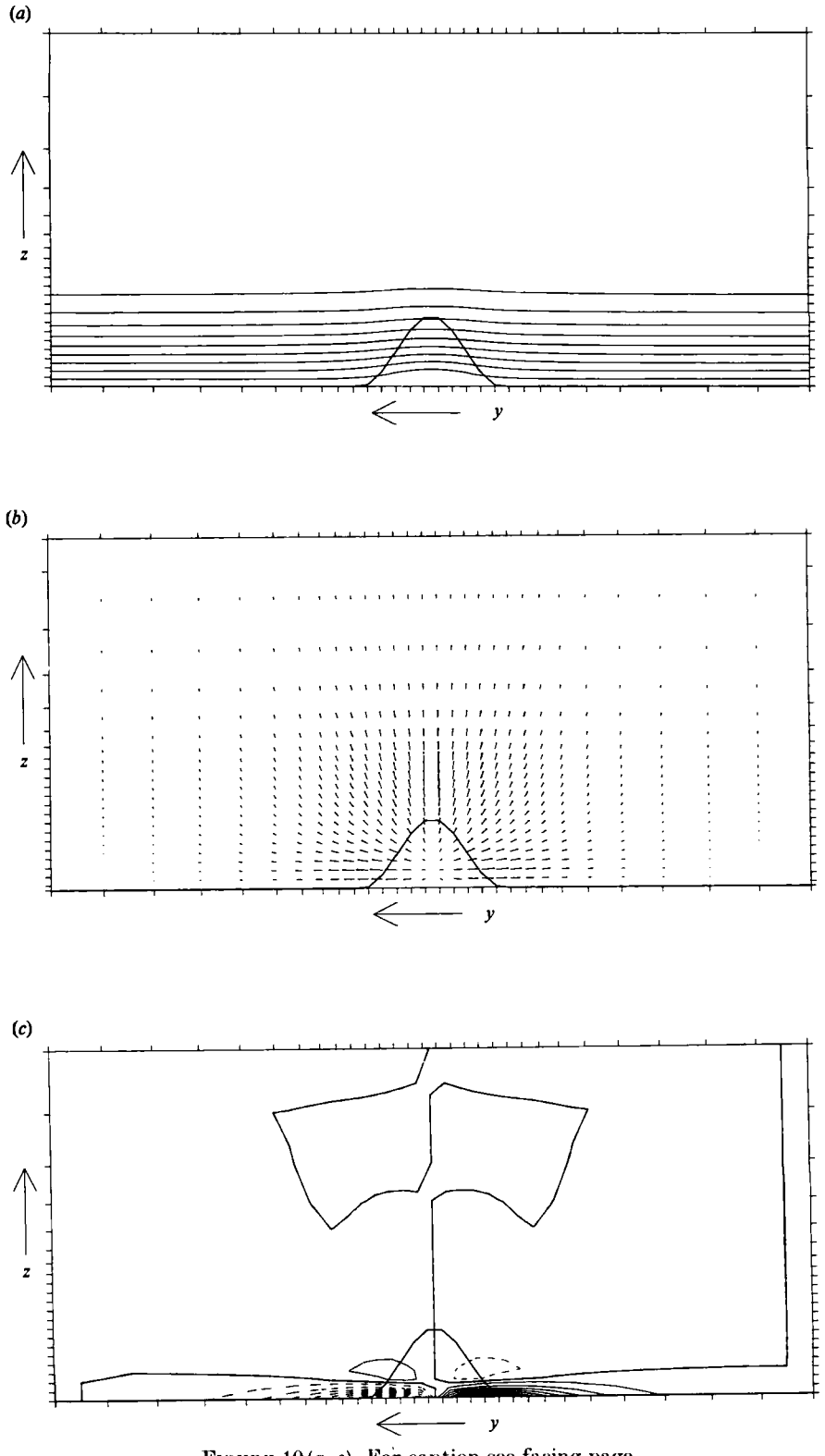

FIGURE 10(*a–c*). For caption see facing page.

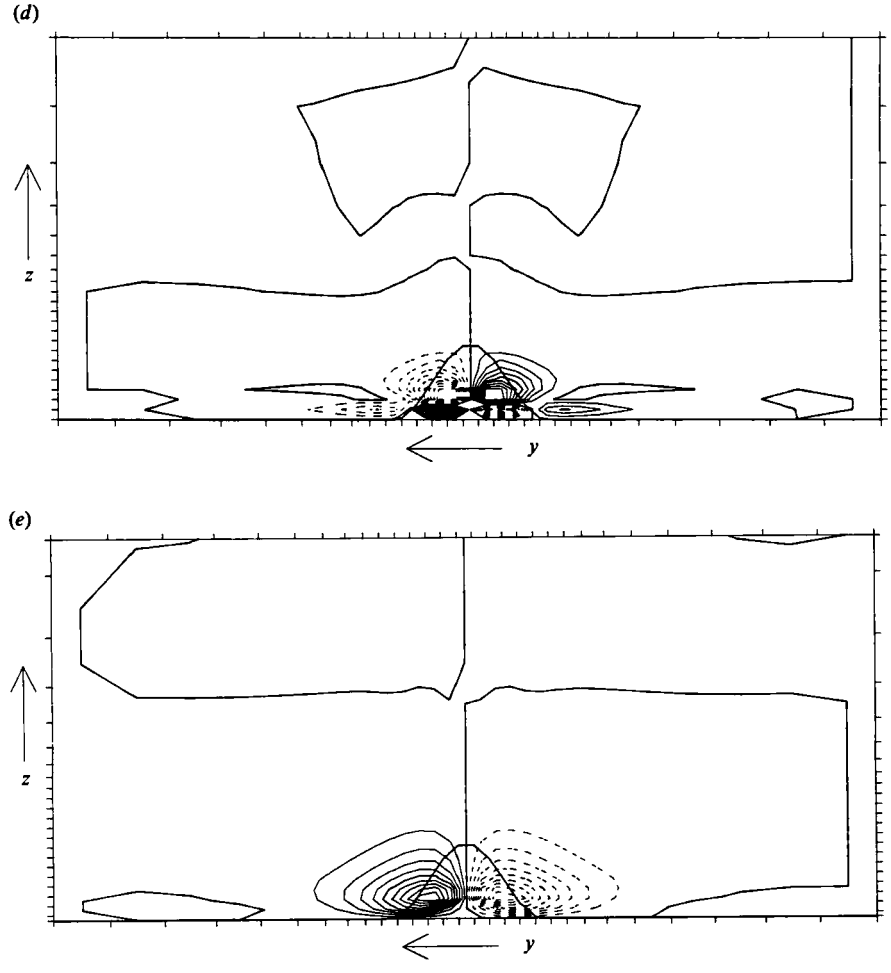

FIGURE 10. Transverse sections at the upstream extremity of the obstacle for case B showing: (*a*) contours of the streamwise velocity component U with contour interval $0.1U$; (*b*) transverse flow vectors with a maximum vertical velocity magnitude $0.025U$; (*c*) contours of ξ with contour interval $0.091U/L$; (*d*) contours of the stretching term $St = \xi(\partial u/\partial x)$ with contour interval $1.2 \times 10^{-3}U^2/L^2$; (*e*) contour of the turning term $Tu = (\partial v/\partial x)(\partial u/\partial z) - (\partial w/\partial x)(\partial u/\partial y)$ with contour interval $1.3 \times 10^{-2}U^2/L^2$. An outline of the obstacle is given in each figure.

extensive flow separation and a reduced basic pressure gradient corresponding to a reduced boundary-layer growth. There are also more marked pressure disturbances associated with the trailing wake but they are too small to be seen in comparison with the main maxima and minima. The surface-stress and centreplane trajectories are shown in figures 9 (*a*, *b*), respectively. There is upstream separation, and extensive lee separation; and the saddle point of the lee surface stress field is seen to be a point of separation. Trajectories are lifted in the separated region and remain aloft downstream. It should be noted that upwash and continuing elevation have been observed in laboratory experiments on laminar flow (e.g. Hunt *et al.* 1978), but have not hitherto been reconciled with the downwash suggested by horseshoe vortices. We shall propose, however, that lee saddles are points of separation or attachment according as the dominant trailing vortices yield upwash or downwash on the downstream plane of symmetry.

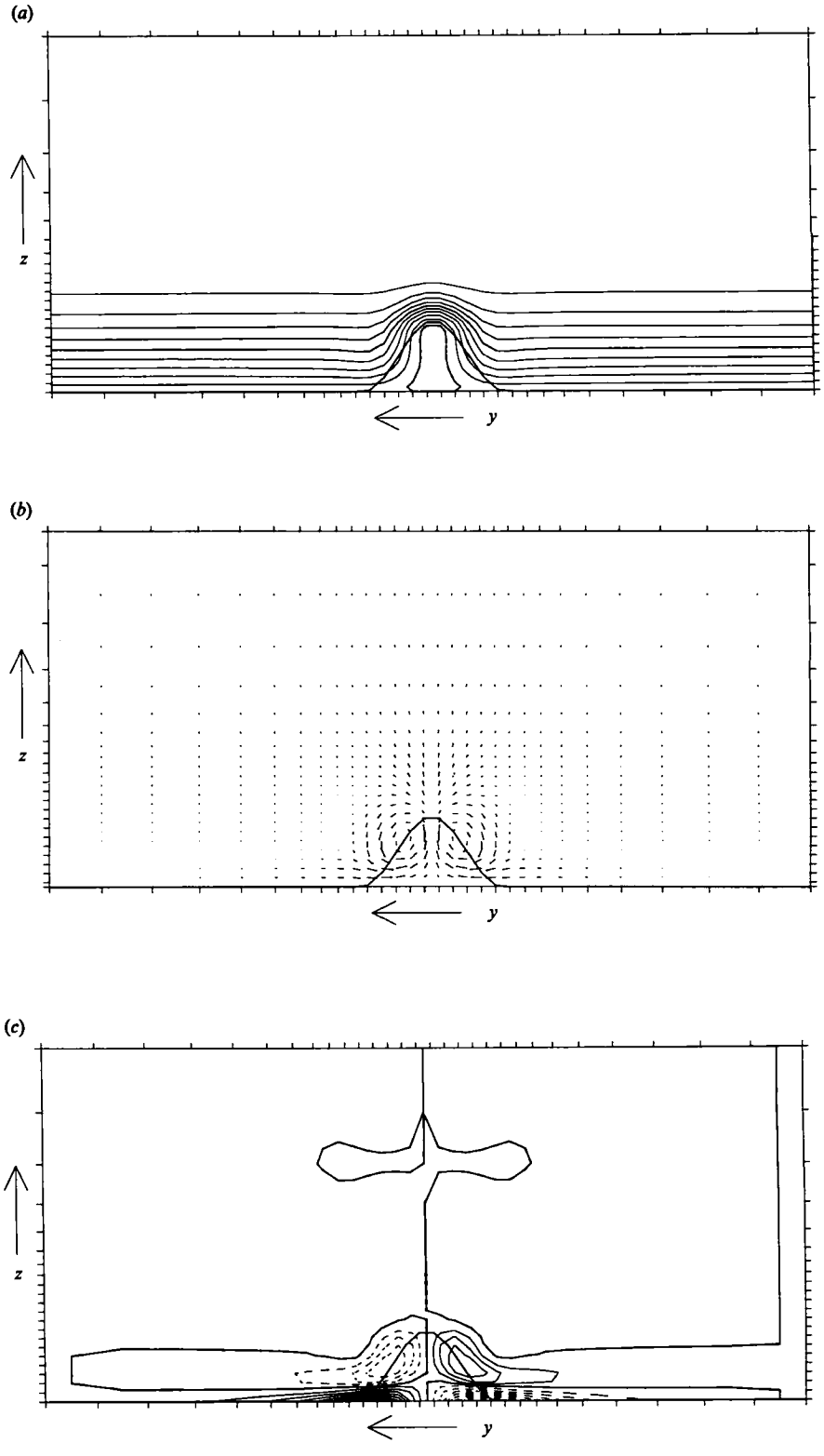

FIGURE 11 (*a–c*). For caption see facing page.

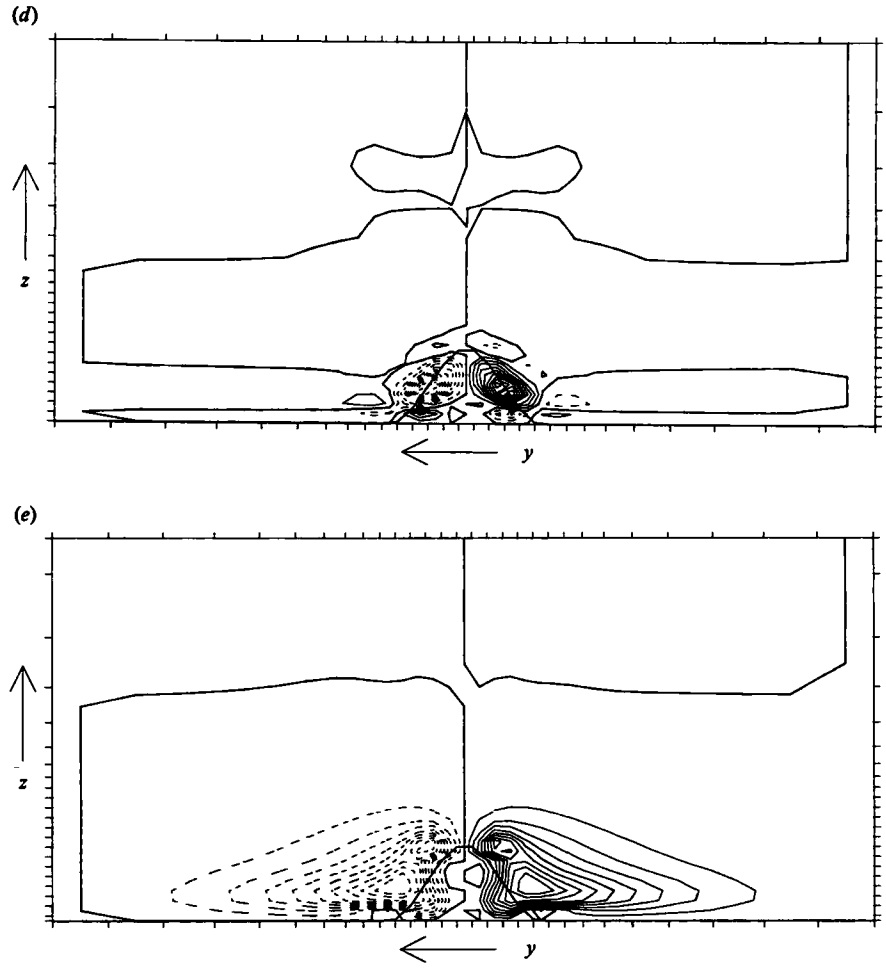

FIGURE 11. Transverse sections at the downstream extremity of the obstacle for case B. As figure 10. (*a*) U with contour interval $0.1U$ (note that the zero contour leaves the surface where the flow reverses); (*b*) transverse flow vectors with maximum vertical velocity magnitude $0.036U$; (*c*) ξ with contour interval $0.113U/L$; (*d*) St with contour interval $4.1 \times 10^{-3}U^2/L^2$; (*e*) Tu with contour interval $5.2 \times 10^{-3}U^2/L^2$. An outline of the obstacle is given in each figure.

Sections of various variables in vertical transverse planes are shown in figures 10–12. These sections are located at each of three stations comprising the upstream edge of the obstacle, its downstream edge, and the downstream end of the computational domain respectively. The variables are (*a*) the streamwise component of velocity, (*b*) the transverse velocity field, (*c*) the streamwise component of vorticity ξ, (*d*) the 'stretching' term $St = \xi \partial u/\partial x$, and (*e*) the 'turning' term $Tu = \eta \partial u/\partial y + \zeta \partial u/\partial z$. The sum of the stretching and turning terms $Tu + St = \boldsymbol{\omega} \times \boldsymbol{\nabla} \boldsymbol{u}$ (where $\boldsymbol{\omega} = \boldsymbol{\nabla} \times \boldsymbol{u} = (\xi, \eta, \zeta)$) is the total inertial processing of streamwise vorticity. Although the thickness of the Blasius boundary layer is the same as that in case A at the upstream edge of the domain, it is evident from the sections that, owing to the higher Reynolds number, it is shallower over the rest of the domain. At the upstream section (figure 10) the disturbance velocity field is broadly similar to that in the lower-Reynolds-number case. The differences appear more clearly in the longitudinal

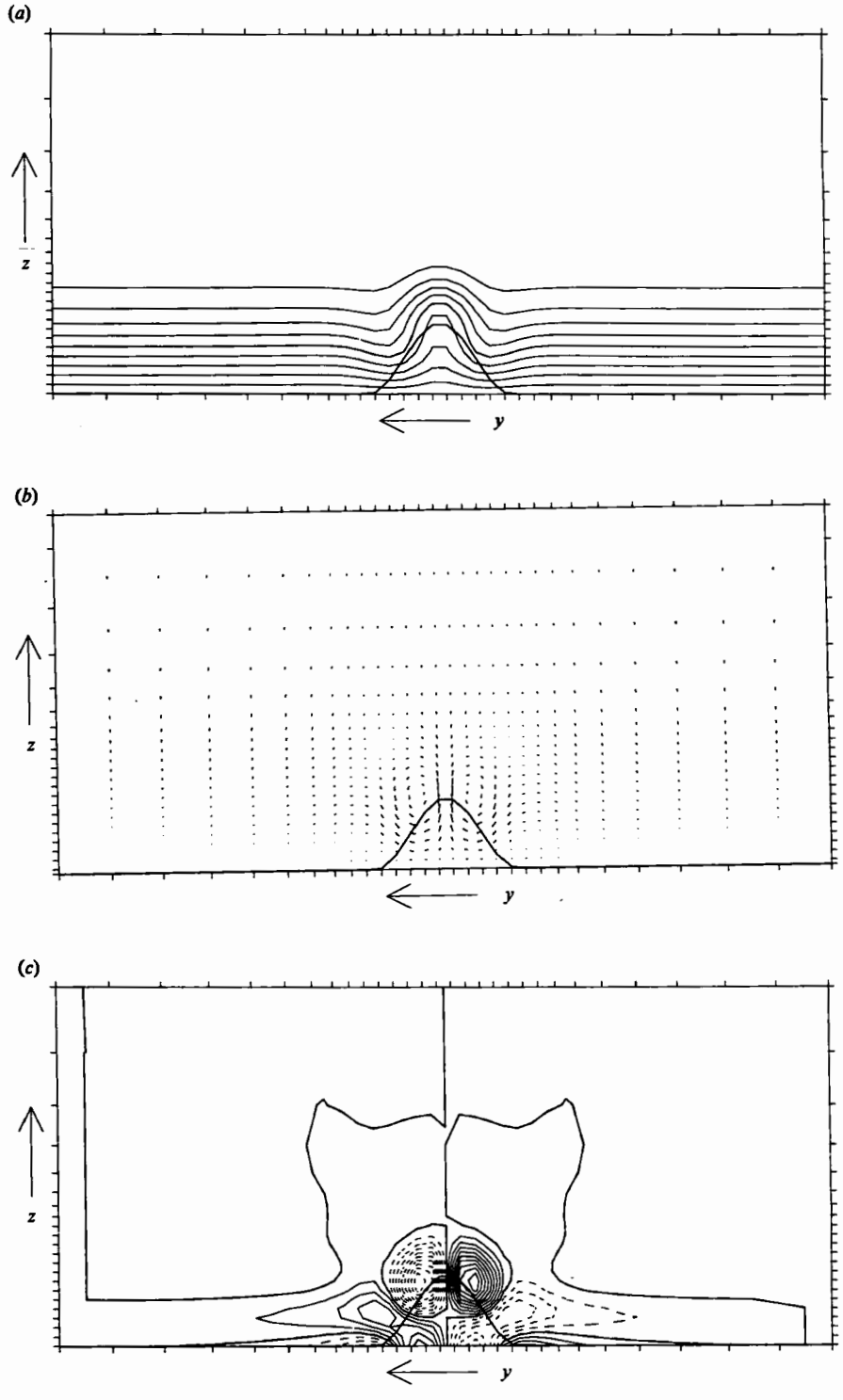

FIGURE 12 (*a–c*). For caption see facing page.

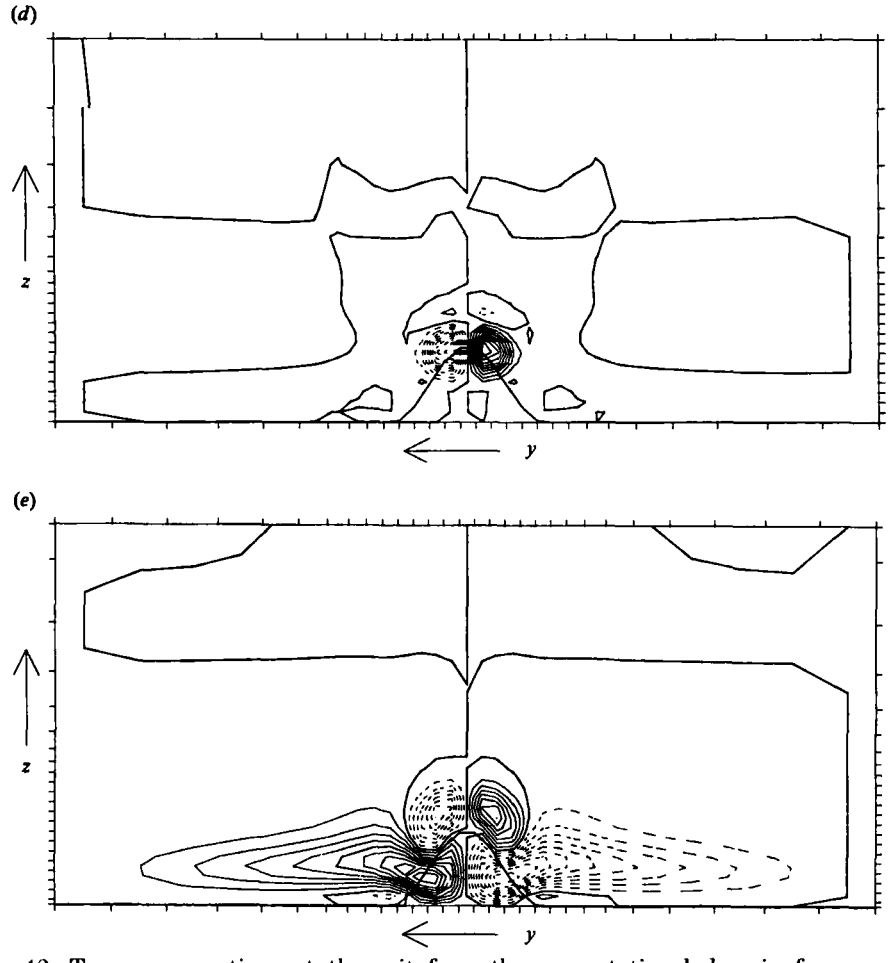

FIGURE 12. Transverse sections at the exit from the computational domain for case B. As figure 10. (*a*) U with contour interval $0.1U$; (*b*) transverse flow vectors with maximum vertical velocity magnitude $0.014U$; (*c*) ξ with contour interval $0.01U/L$; (*d*) St with contour interval $1.4\times10^{-4}U^2/L^2$; (*e*) Tu with contour interval $2.4\times10^{-4}U^2/L^2$. An outline of the obstacle is given in each figure.

vorticity field (figure 10*c*) where the reduced relative diffusion results in a thinner lower-level pair arising from vorticity generated in the pressure gradient over the lower boundary and reduced cross-diffusion between the upper and lower vortex pairs. Because the upper vortex pair is older and more diffuse than that near the boundary, the contouring procedure with contour interval one-tenth of the maximum vorticity in the section tends to distort the balance between upper and lower vortices. A global representation of the ξ-field is provided by the circulation $-0.033UL$ in the left-hand (y,z)-quadrant, and the streamwise ξ flux $+0.0031U^2L$ through the same quadrant. This sense of net circulation corresponds with upwash on the upstream plane of symmetry and shows that the lower, freshly generated vortex pair is stronger in total, although not much stronger as the ξ-flux is of opposite sign because the advection velocity increases with distance from the boundary. The stretching term St at this location is less than a tenth of the turning term Tu and is mainly due to the flow deceleration ahead of the obstacle. It tends to reduce the vorticity magnitude

at this location. The turning component has a dipole structure corresponding to the expected turning of the basic transverse boundary-layer vorticity.

In the transverse section at the downstream edge of the obstacle (figure 11) the wake is now stronger and narrower because of the reduced importance of diffusion relative to advection, and there is weak reversed flow within the $u = 0$ contour. The transverse velocity-vector array shows a dominant trailing-vortex pair with central upwash and symmetrical lateral downwash (figure 11*b*). A comparison with figures 10 (*b*) and 7 (*b*) shows that the vortex wake is narrower than the corresponding upstream disturbance, and appreciably narrower than the lower-Reynolds-number wake at the same station. Near the surface the contours of streamwise vorticity (figure 11*c*) show a strongly concentrated lower-level vortex pair still suffering active generation as the pressure field accelerates flow into the wake. Above this surface concentration there is the vortex pair corresponding to the circulation seen in the transverse velocity vectors. This has the same sense as the pressure-generated pair seen adjacent to the surface upstream of the obstacle. Above this vortex pair, but too weak to appear in the contour plot, is a very weak upper-level vortex corresponding with the surviving turned basic boundary-layer vorticity. At this location the vorticity generated upstream is widely dispersed and largely annihilated by cross-diffusion. The features dominating figure 11 (*c*) are due to recent production downstream of the summit of the obstacle. The net circulation in the left-hand (y, z)-quadrant is $-0.029UL$ and the ξ-flux is $-0.0019U^2L$: this corresponds with net upwash on the symmetry plane. These are, however, only residual values representing the difference between much larger opposed contributions from the three levels, the middle-level vortices alone having one-sided circulation approximately *seven times* that in the quadrant ($\approx 0.2UL$), while ξ takes a peak value $\approx U/L$. Noting that a relevant local velocity scale is $\bar{u} \approx 0.4U$ it is evident that both the individual circulations and the typical transverse velocities ($\approx 0.1\bar{u}$) are comparable with those observed in high-Reynolds-number turbulent flow (e.g. Hansen 1975). Although, for the Reynolds number considered here, the flow perturbation increases rapidly with Reynolds number this tendency must cease with the onset of fully developed turbulent flow. In the latter case the effective turbulent diffusivity will have a different character but is likely to be comparable in magnitude with that in the present moderate-Reynolds-number flow. The fields of St and Tu at this location show two effects of similar magnitude. The stretching term St arises from the streamwise flow acceleration in the wake and is seen (figure 11*d*) to promote the concentration of the dominant mid-level vortex pair. The turning term Tu (figure 11*e*) shows a larger distribution as the transverse vorticity of the wake and boundary layer to the side of the obstacle is advected. The sense of turning is opposite to that seen upstream and is related to flow over the centreplane of symmetry being faster than flow to the sides of the obstacle.

An examination of sections between those of figures 10 and 11 shows that upstream of the summit a qualitative resemblance to the structure seen in figure 10 persists. Downstream of the summit there is a qualitative resemblance to the flow seen in figure 11 but the maximum vorticity production owing to turning is closer to the surface. The generation of the mid-level vortex pair dominating the wake is mainly due to turning occurring downstream of the summit. The turning occurs as vorticity transverse to the stream and relatively close to the surface of the obstacle is sheared by transverse gradients of the longitudinal flow, this vorticity having been generated principally by the strong streamwise pressure gradient behind the upstream stagnation point. The sign of the inertial turning is determined by the sign of these

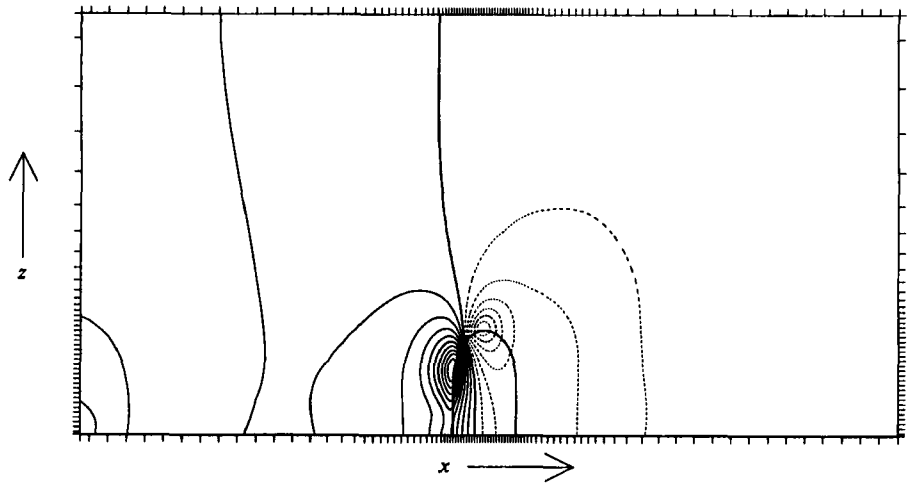

FIGURE 13. Pressure field for case C in a streamwise section through the centre of the body. The field has an arbitrary zero value; negative values are denoted by dashed contours and the contour interval is $0.046U^2$.

transverse gradients of longitudinal flow over the obstacle, and upwash vortices appear in this case to be a consequence of the flow maximum on top of the obstacle.

At the exit section, five obstacle diameters downstream the longitudinal velocity in the wake shows appreciable distortion relating to the dominant vortex pair (figure 12*a*). The pair itself is still clearly visible in the transverse velocity field (figure 12*b*) although it has lifted, spread and weakened, with the maximum vertical velocity falling from $0.0356U$ to $0.014U$. The ξ-field has also weakened (figure 12*c*) with the maximum vorticity ξ_{max} decreasing from $1.13U/L$ to $0.103U/L$ (it should be kept in mind that the contour spacing is $0.1\,\xi_{max}$, decreasing with ξ_{max}). The dominant pair still has individual circulation seven times that of the quadrant and has central upwash. The lower-level structure is now more complex. The remnants of the lower-level pair seen just behind the obstacle are seen as a diffuse pair to the sides. The pressure field at the boundary has a weak high under the downflow on either side of the dominant vortex pair and a central low. This results in the generation of weak line doublets on either side of the centreplane. One reason for the weakening of the low-level vortex pair apparent in the section at the downstream edge of the obstacle is the role of the middle-level pair in drawing a thin stream of lower-level fluid up the centreplane, where the contributions of vorticity from right and left are likely to annihilate each other in considerable measure. The local generation of ξ by the action of stretching (figure 12*d*) shows that the continuing acceleration of the streamwise flow is still significant. In contrast the local generation of ξ by the action of turning (figure 12*e*) is more complex than immediately behind the obstacle. This complex structure arises from the distortion of the wake so as to give velocity maxima at the sides of the wake where downflow occurs. The combined field of inertial processing shows a nearly equal tendency to reinforce both the dominant vortex pair and the lower vortex pair and confirms that the weaker strength of the lower pair must stem from increased annihilation.

Figures 13–18 show solution fields for case C. The Reynolds number, 108, is similar to that of case B and just below that at which the flow becomes unsteady. Owing to the vertical sides to the obstacle the surface pressure is hard to display and instead

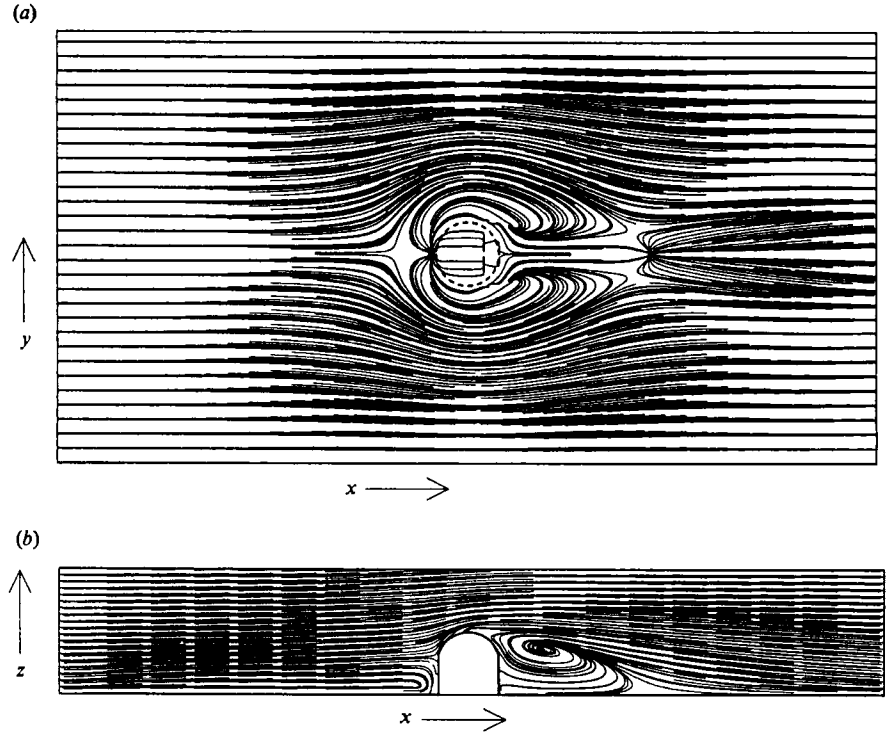

FIGURE 14. Flow directions for case C: (*a*) surface stress pattern and (*b*) streamwise section in the centre plane. For economy only the part of the flow below $z = 2h$ is illustrated.

a vertical streamwise section through the centre of the body is illustrated (figure 13). The main features are the expected maximum on the upstream face and minimum over the summit. The obstacle is bluff and taller than the undisturbed-boundary-layer depth so the pressure maximum $0.463U^2$ is close to the value ($\frac{1}{2}U^2$) expected for a stagnation point in an inviscid flow. Owing to the different parameters, the fractional change in the boundary-layer depth as the flow travels through the domain is larger than in cases A and B and the resulting pressure disturbance is correspondingly greater. As before this pressure disturbance is due to the finite depth of the domain and is most marked where the rapid growth of the boundary layer occurs at the inflow. The surface-stress and centreplane trajectories are shown in figures 14(*a*,*b*) respectively. As in case B there is an upstream separation, and an extensive lee separation; in contrast to case B the saddle point of the lee surface stress field is seen to be a point of attachment. The vertical section shows that the lee separation is characterized by a spiral mode with downwash remote from the body. Upwash occurs only immediately behind the body. This flow structure is consistent with a trailing-vortex pair with downwash. Previous examples (Hunt *et al.* 1978, figure 16*b*) of the flow structure associated with downwash have been for turbulent rather than laminar flow and have a quite different topology. In their example a streamline from the summit of the hill ends in the spiral node, and the rear separation is the point of attachment for a streamline starting upstream. In the present case the rear separation is also a point of attachment but the attaching streamline does not originate upstream but in a spiral node which is a source rather than a sink. Flow lines from the summit of the hill and above move steadily towards the surface far downstream of the region

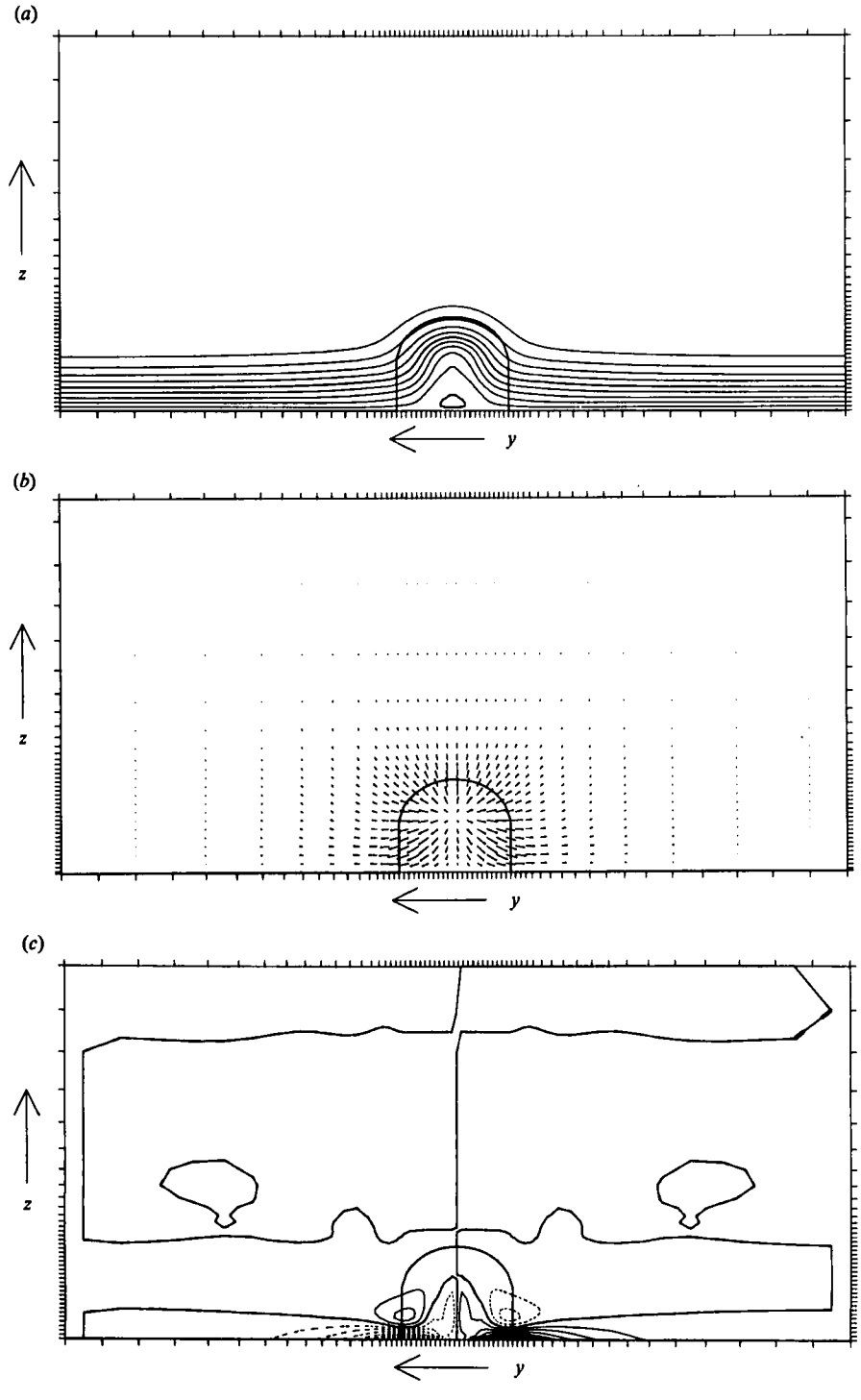

FIGURE 15. Transverse section $0.1L$ upstream of the upstream extremity of the obstacle for case C, showing (*a*) contours of the streamwise velocity component U with contour interval $0.1U$, (*b*) transverse flow vectors with a maximum vertical velocity magnitude $0.321U$ (in this case a vector has been drawn from alternate grid points), (*c*) ξ with contour interval $0.27U/L$. An outline of the obstacle is given in each figure.

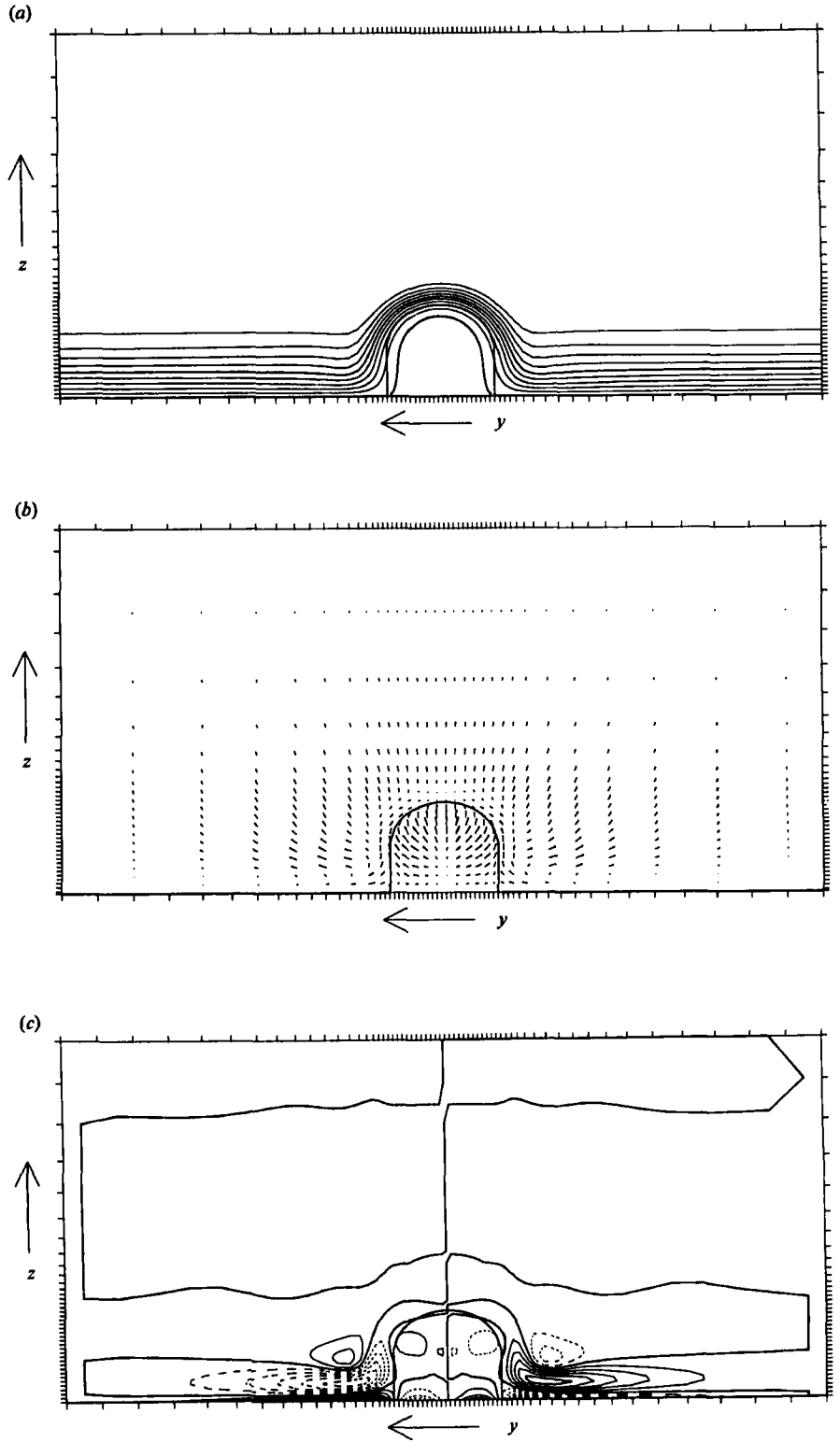

FIGURE 16(*a–c*). For caption see facing page.

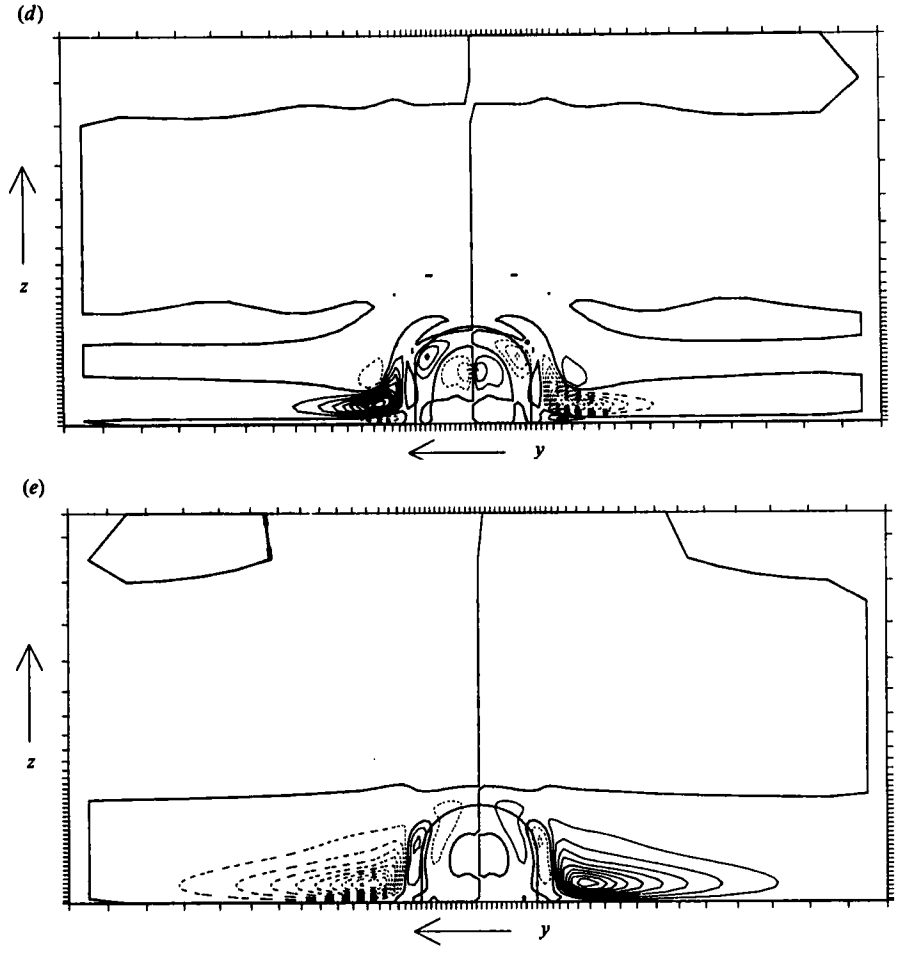

FIGURE 16. Transverse sections $0.1L$ downstream of the downstream extremity of the obstacle for case C. As figure 15. (*a*) U with contour interval $0.1U$; (*b*) transverse flow vectors with maximum vertical velocity $0.071U$; (*c*) ξ with contour interval $0.047U/L$; (*d*) St with contour interval $0.0045U^2/L^2$; (*e*) Tu with contour interval $0.0102U^2/L^2$. An outline of the obstacle is given in each figure.

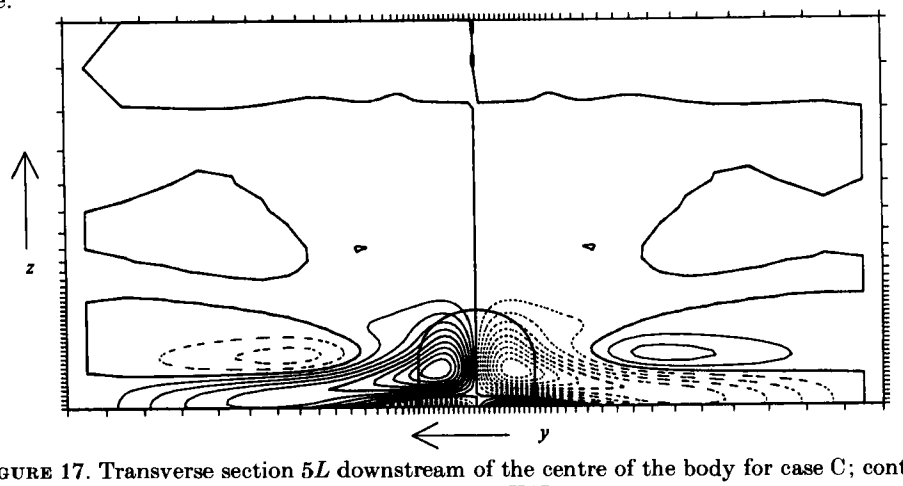

FIGURE 17. Transverse section $5L$ downstream of the centre of the body for case C; contour interval $0.099U/L$.

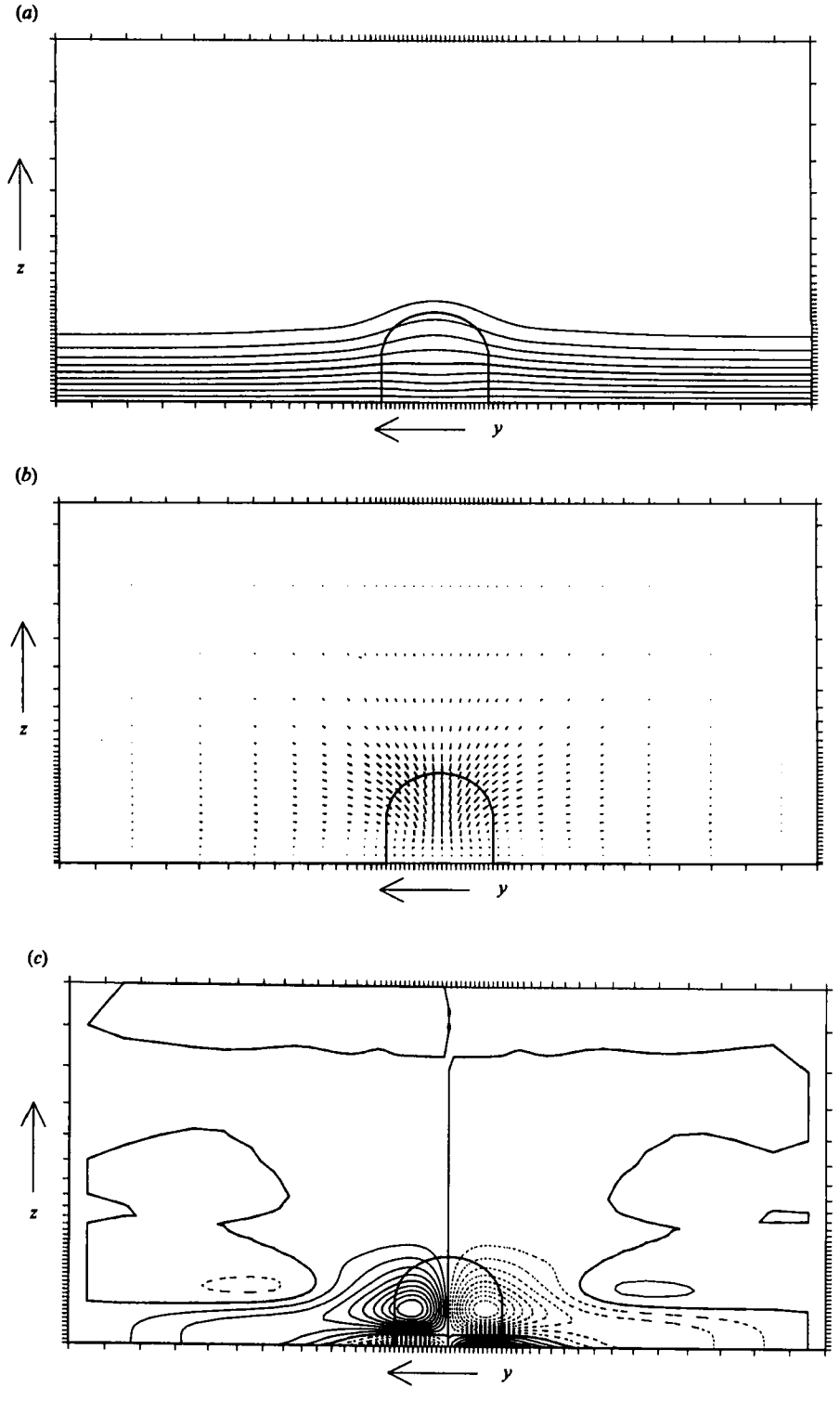

FIGURE 18. Transverse sections at the exit from the computational domain for case C. As figure 15. (*a*) U with contour interval $0.1U$; (*b*) transverse flow vectors with maximum vertical velocity $0.054U$; (*c*) ξ with contour interval $7.1 \times 10^{-3}U/L$. An outline of the obstacle is given in each figure.

of flow separation. It is evident that our understanding and knowledge of possible flow structures is limited and more work, especially in observations, is needed.

Sections of various variables in vertical transverse planes are shown in figures 15–18. The sections are located at $x = -1.1L$, $+1.1L$, $5.0L$, and $13.0L$, where the centre of the object is at $x = 0$. At the upstream section (figure 15) the streamwise velocity field (figure 15*a*) shows a region of reversed flow. The transverse velocity vectors (figure 15*b*) show a flow radiating out from the elevated pressure maximum. At the surface this radial flow is deflected outward. The field of the streamwise component of vorticity ξ is qualitatively similar to that in the corresponding section in case B but the upper vortex pair arising from the turning of the transverse boundary-layer vorticity is more intense. The increase in intensity is due to the obstacle being both bluff and taller than the local boundary depth. As before the net circulation in each quadrant is very much smaller than the circulation associated with individual vortices. Owing to the greater flow separation and more complex transverse vectors the inertial-generation terms (not shown) are a little more complex than those in case B. However outside the region near the surface and axis of symmetry, the dominant inertial processing is still the expected turning of basic boundary-layer vorticity to produce a vortex pair with downwash.

In the section at the downstream edge of the obstacle (figure 16*a*) the wake is seen to be close in size to the outline of the obstacle. The transverse flow vectors (figure 16*b*) show a more complex pattern than those in case B. Although upwash dominates the flow near the wake it is clear that the vorticity distribution is more complex. The field of the streamwise component of vorticity (figure 16*c*) confirms this but shows some striking similarities with the corresponding field in case B. To the side of the wake the structure is qualitatively as in case B but the surviving turned basic boundary-layer vorticity has retained its relative magnitude. It is still small in relation to the underlying vortex pair with upwash. As with case B this upwash pair has arisen mainly from inertial turning occurring to the sides of the body. Beneath the upwash pair is a downwash pair suffering generation as the pressure field accelerates flow in towards the wake. The main differences from case B occur inside the wake. Here there are weaker distributions of vorticity. The inertial-generation terms confirm this picture. To the side of the wake these are as in case B but inside the wake there are important differences. The main extra feature is the generation of a downwash pair within the nearly vertical shear layer comprising the sides of the wake. This generation of a downwash pair in the shear layer is maintained for some distance downstream and spreads in lateral extent as the wake diffuses. At $5L$ downstream (figure 17), a location downstream of the rear saddle point in the surface stress field, there has been considerable mutual annihilation of the various vortex pairs and an apparent merging of the downwash pair generated in the shear layer with the downwash pair generated by pressure gradients to the sides of the wake. This feature dominates the flow and the contribution of the surviving turned basic boundary-layer vorticity is elevated – and very small.

At the exit section (figure 18), about $12L$ downstream, the wake shows both collapse and some modification due to the dominant vortex pair with downwash. The transverse velocity vectors show that the circulation is not strong relative to the tendency for the wake to collapse. The vorticity field is similar to that seen at $x = 5L$; the downwash pair is seen to remain concentrated. As with case B the generation is becoming more complex as the wake is distorted by the action of the trailing vortices. We can anticipate that in flows at higher Reynolds numbers these distortions and subsequent changes in vorticity generation will be more important. The difference

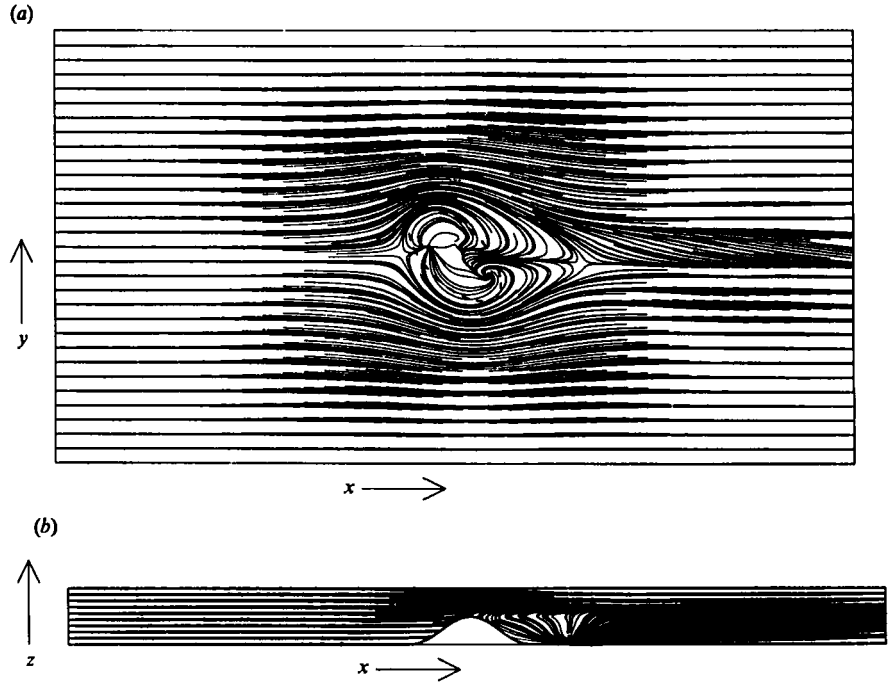

FIGURE 19. Flow directions for case D: (*a*) surface stress pattern, and (*b*) streamwise section in the centreplane. For economy only the part of the flow below $z = 2h$ is illustrated.

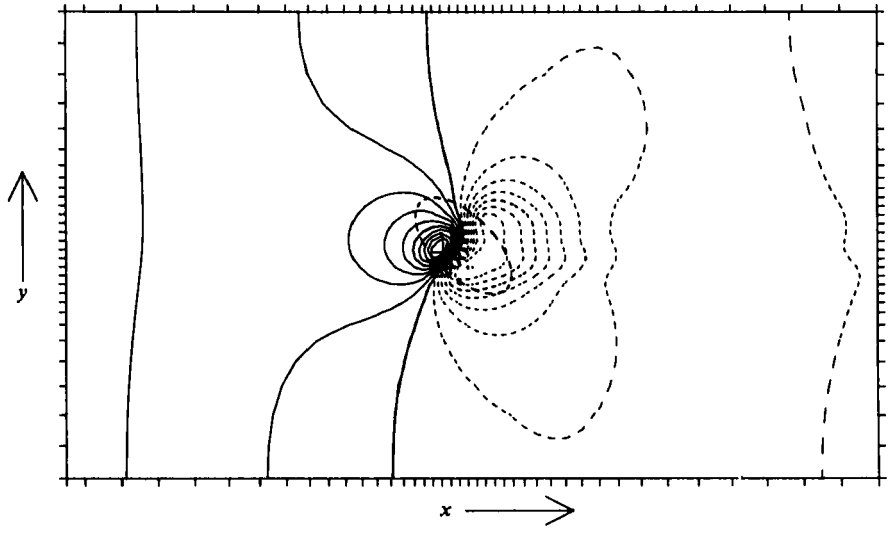

FIGURE 20. Surface pressure field for case D. Contour interval is $0.0064U^2$. See figure 4 for plotting convention.

between the trailing-vortex structures found in cases B and C clearly indicate the importance of body shape. In case C the domination by a single vortex pair is less clear cut. From the results of the laboratory study presented below it seems likely that this is due to the object used in case C being fairly 'neutral' in shape and not dividing the flow so laterally as, for example, a taller object. Unfortunately an object

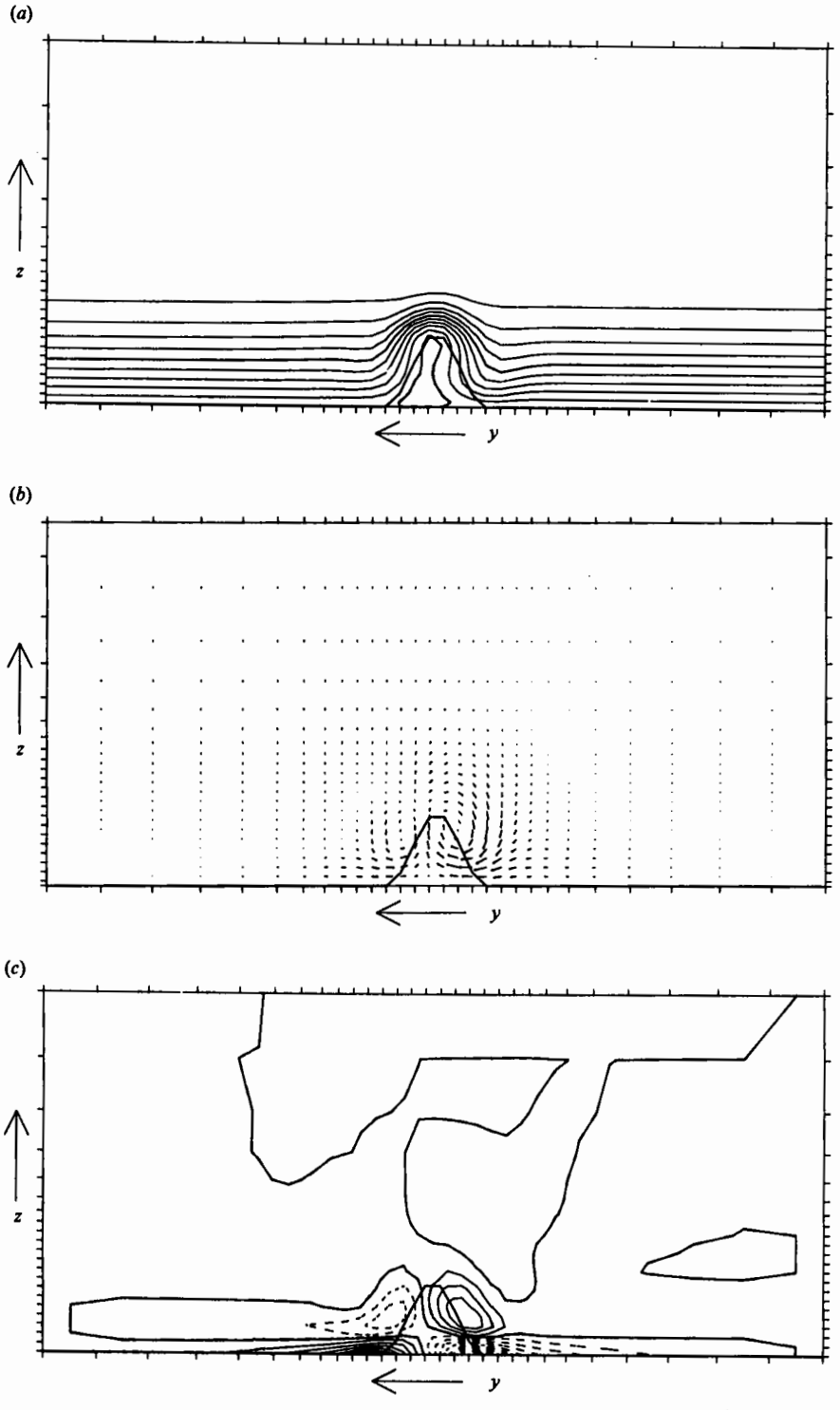

FIGURE 21. Transverse sections at the downstream edge of the obstacle for case D. As figure 6. (*a*) U with contour interval $0.1U$, (note that the zero contour leaves the surface where the flow reverses); (*b*) flow vectors with maximum vertical velocity magnitude $0.048U$; (*c*) ξ with contour interval $0.14U/L$.

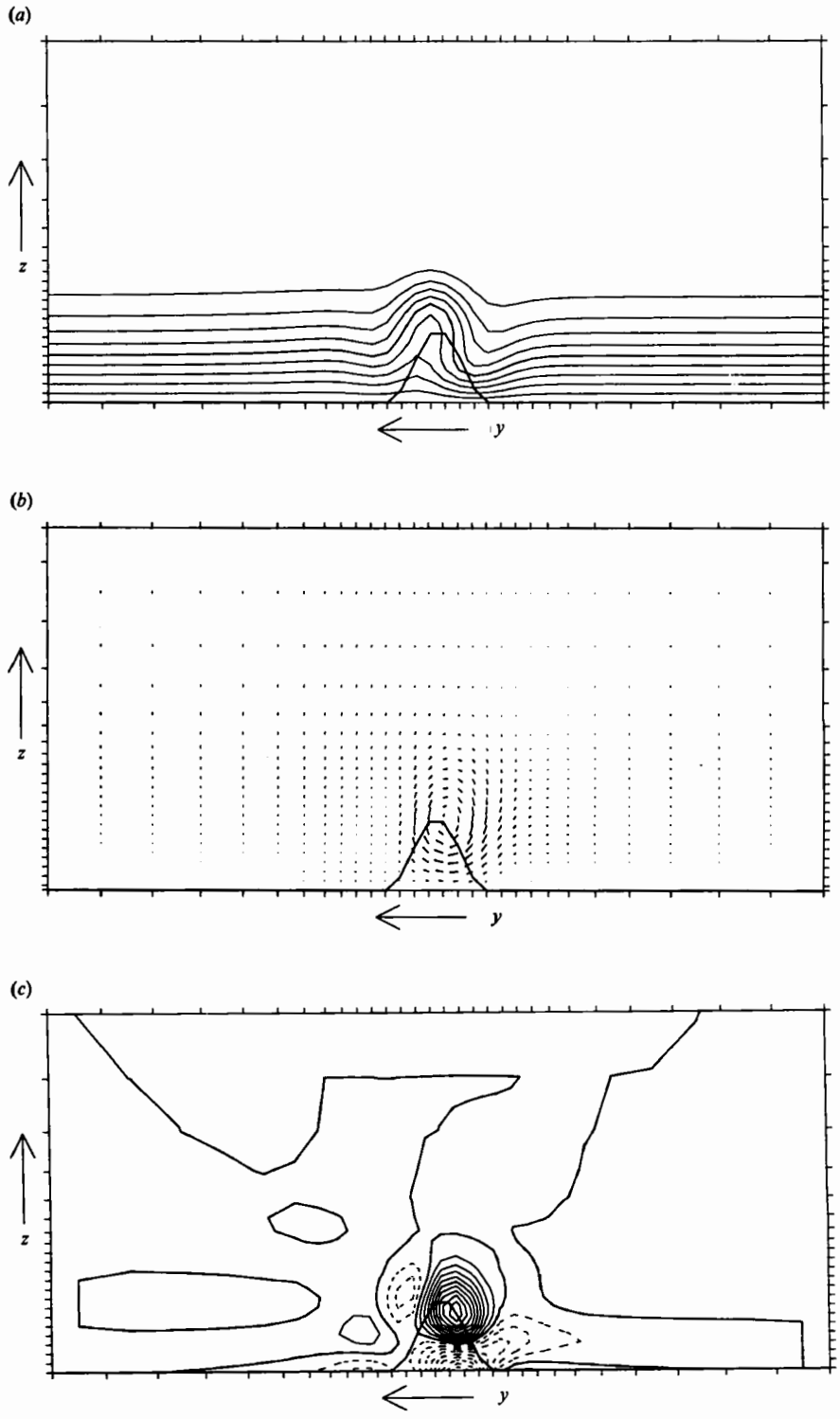

FIGURE 22. Transverse sections at the exit from the computational domain for case D. As figure 6. (*a*) U with contour interval $0.1U$; (*b*) flow vectors with maximum vertical velocity magnitude $0.021U$; (*c*) ξ with contour interval $0.023U/L$.

either with greater height or with a flow with a thinner boundary-layer depth is beyond the computational resources available for this work.

3.2. *Vortex wakes of asymmetric obstacles*

The final model run to be reported is case D for an obstacle with the same parameters as case B except that it has elliptical horizontal sections with the major axis inclined at $+45°$ to the undisturbed stream. The surface stress field and flow trajectories in the vertical centreplane are shown in figures 19(*a*, *b*) respectively. The flow over and behind the obstacle is clearly asymmetric, but with broadly similar separation features to those of case B. The wake is dominated by a single trailing vortex, as shown by the cross-flow visible downstream in the surface stress field. The central longitudinal section ($y = 0$) is no longer a plane of symmetry, but the trajectories have the same structure as those for the symmetrical case B. Examination of the surface pressure field (figure 20) also shows a similarity to case B but asymmetry, in the sense expected for a lifting body (section of an aircraft wing), is evident. Transverse sections of the flow field are shown in figures 21 and 22. The upstream sections are not included as the flow asymmetry is slight and the contours differ little from those for case B. Downstream, however, as shown in the transverse sections at the rear edge of the obstacle (figures 21*a*, *b*, *c*) and at the end of the computational box (figures 22*a*, *b*, *c*), the asymmetry is pronounced. Immediately behind the obstacle the contours of streamwise velocity (*a*) are a little tighter and displaced to the true left of the centreplane but showing little obvious sign of asymmetric rotation. The asymmetry shows more clearly in the transverse velocity field (*b*), where the right-hand vortex is displaced to the left but otherwise appears little changed, while the left-hand vortex is appreciably weakened. The streamwise vorticity field shows that there is still a dominant vortex pair at this station just downstream of the obstacle. Examination of the fields of inertial generation of ξ at this location, St and Tu (not shown), show a similar apparently small departure from symmetry. The inertial generation has the same basic character as the fields in case B.

In the whole transverse section the gross circulation is $+0.013UL$ which is in magnitude only about $\frac{1}{40}$ of that in each core separately. This gross circulation is non-zero only because there is a pressure difference laterally across the computational box. Ideally a 'lifting' obstacle experiencing transverse force should generate an opposing lateral flux of momentum in passing fluid, and if the lateral boundaries are far enough away the appropriate boundary conditions will be zero disturbance pressure and a cross-flux of momentum (initially unknown). This computational model, however, assumes mirror-image conditions at lateral boundaries and therefore no cross-flow but instead a reduction in pressure on the sidewall towards the face of the obstacle and a corresponding increase in pressure on the side away from it. This net difference in pressure across the box will cause a net generation of vorticity over the lower boundary and hence a progressive change in circulation with increasing distance downstream. Here the high is to the left and low to the right, and there is progressive generation of positive streamwise vorticity.

Figures 22(*a*, *b*, *c*) show sections of the flow as it exits at the downstream end of the computational domain. In spite of the weak asymmetry just behind the obstacle the flow is strongly asymmetric by this stage. The streamwise velocity contours now show signs of clockwise twisting in the wake (figure 22*a*) and there is a single dominant trailing vortex in the transverse velocity field (figure 22*b*). The vorticity field (figure 22*c*) confirms the dominance of this single circulation and shows it to be located above a region of vorticity of opposite sign. The other vortices seen in

figure 21(*c*) have suffered a considerable mutual annihilation as they have been advected around the dominant vortex. The stretching and turning terms in the equation for streamwise vorticity show that the reinforcement of the dominant vortex occurs mainly through the stretching term. Near the surface the presence of a velocity maximum on the right-hand side of the wake causes a concentrated region of turning. This has a sense opposite to the dominant vortex, and mutual annihilation will occur. The rate of decay of the peak vorticity, $\xi_{max} = 1.4U/L$ in the section just behind the obstacle and $\xi_{max} = 0.23U/L$ at the edge of the domain, is less than with the vortex pair in case B. This is consistent with the larger scale of the vortices within the 'single' vortex flow.

4. The laboratory experiments

The four cases simulated numerically have yielded a considerable amount of information, but it has only been possible to cover a limited range of parameters. Where novel concepts are involved, it is important to provide an independent test of numerical simulations by a controlled laboratory experiment, and so a series of simple experiments was carried out on flow past a variety of obstacles in a water channel. Flow in the wakes of obstacles is at least unsteady and generally turbulent except at relatively low Reynolds numbers, and sophisticated measurement techniques and data analysis are needed to identify vortex structures in unsteady or turbulent wakes. We are thus forced to confine our attention to low and moderate Reynolds numbers. A disadvantage of this is the dependence on Reynolds number of the location of flow separation on bluff bodies. In the numerical model the treatment of bodies with sharp edges would require enhanced resolution and the numerical results shown above depend on the Reynolds numbers. In the laboratory study this Reynolds-number dependence can be minimized by adopting bodies with plane faces and sharp edges so that separation is determined by body geometry and not Reynolds number. Thus there are limitations on both the numerical and the laboratory experiments but the two complement each other with the simulations providing specific details and the experiments giving confirmation of the application of the conceptual model to a wide range of body shapes.

The experiments were carried out in a small recirculating water channel with working section approximately 200 mm long, 120 mm wide and 120 mm deep. At the operating speed used, 4 mm s^{-1}, the sidewall boundary layers were up to 20 mm thick and the upper surface, although nominally free, was usually locked with contaminants and also supported a boundary layer up to 20 mm thick. The boundary layer on the floor of the channel was poorly defined and a false floor was inserted with a sharpened leading edge facing upstream, allowing a free working depth not less than 80 mm. In operation this plate was inclined slightly to prevent separation from the leading edge, and it supported a thin boundary layer of known properties under a uniform stream. Obstacles were then mounted at distances behind the leading edge with a selected ratio of object height to boundary-layer thickness. This experimental configuration is illustrated schematically in figure 23. The tendency for the channel to increase in width downstream of the leading edge is an incidental feature of the apparatus. In a previous application it compensated for the growth of sidewall boundary layers; here it only acts in this fashion to limited degree. The important point is that the flow in interior was, as noted below, observed to be uniform.

The thymol-blue technique of flow visualization is suitable for the range of speeds considered. The channel was filled with a solution of thymol-blue pH indicator

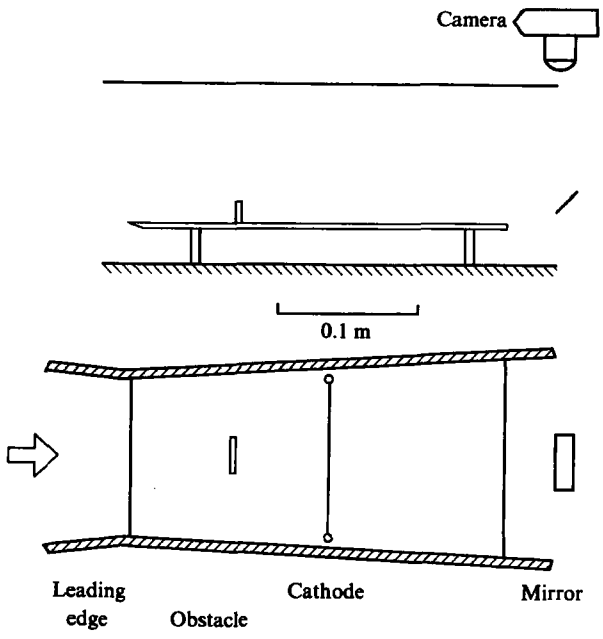

FIGURE 23. Schematic plan and elevation of the water channel working section.

buffered just to orange, and a 25 μm platinum wire served as the cathode with a remote flow-straightening metal grid as the anode. The platinum wire was placed transverse to the stream and parallel to the false floor at a location downstream of the region of reversed flow behind the obstacle. It produced transient lines of blue dye on application of short pulses of voltage between the electrodes. Measurements were taken by observing the dye through a cathetometer and timing the advection of dye over fixed distances. Visual records were obtained (and are reproduced in figures 24 and 25) by photographing the dye traces from downstream of the obstacle using a camera mounted above the free surface and a small inclined mirror suspended in the water far downstream of the obstacle. Photographs 24(*a*) and 25(*a*) in particular show cases of dye traces released from the cathode in the absence of any obstacle, and these confirm the uniformity of the stream.

4.1. *Vortex wakes of symmetrical obstacles*

A variety of upright and sloping rectangular plates and other bodies were used in the experiments and are illustrated in figure 26; and a summary of the principal observations is given in table 2. The channel was operated at uniform speed $U = 4$ mm s^{-1} for all observations, with stream Reynolds number of 100 based on the typical lengthscale 25 mm. Two body locations of 50 and 200 mm downstream of the leading edge of the base plate were used. At these locations the local boundary-layer thickness was measured to be about 7.4 and 15 mm, slightly greater than the theoretical values of 6 and 12 mm expected in an ideal Blasius flow. In addition to the photographs from downstream which show the broad structure of the disturbance flow in sections normal to the stream, a series of measurements was taken of vertical velocity in the plane of symmetry downstream of the obstacle. A representative value of the disturbance velocity on a transverse plane can be obtained using the fact that the vertical speed always has a maximum on the plane of

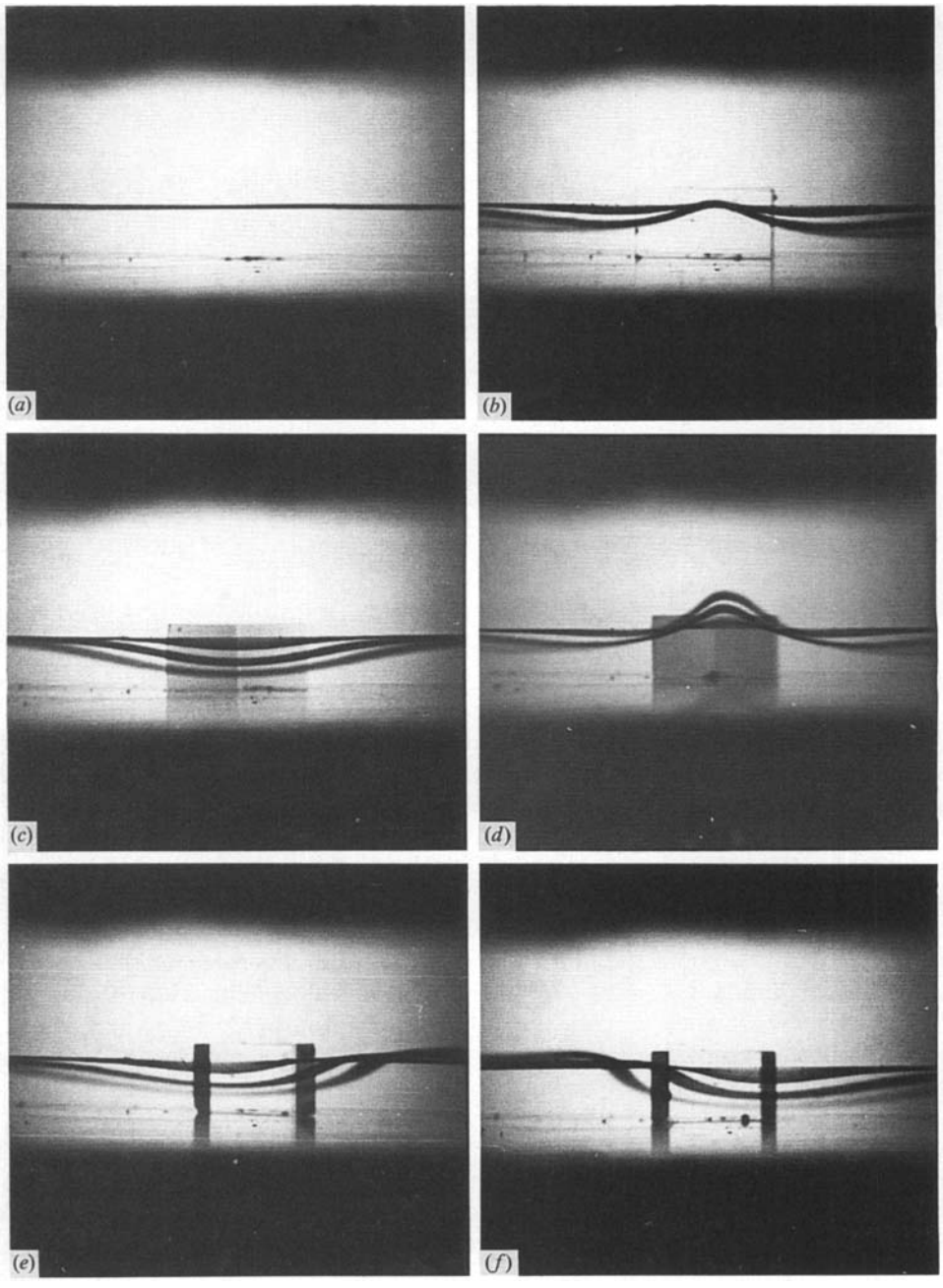

FIGURE 24. Photographs of periodic dye releases from a transverse wire 75 mm downstream of a variety of obstacles standing in the 'thin' ($\delta = 7.4$ mm) boundary layer and viewed from an effective distance of about 400 mm downstream. The time interval between dye releases is 30 s and the initial dye line has travelled about 250 mm when the photographs are taken shortly after the third dye release, which indicates the position of the wire. There is significant perspective distortion, but not so as to invalidate the clear evidence of trailing-vortex pairs. The photographs show the vortex wakes for a series of broad low obstacles, apart from (*a*) which shows the undistorted dye line in the absence of an obstacle: (*b*) the 2×1 rectangle (ii); (*c*) the prism (xi); (*d*) the re-entrant block (xii); and (*e*), (*f*) plate (ii) turned about its vertical axis of symmetry through $+45°$ and $-45°$ respectively.

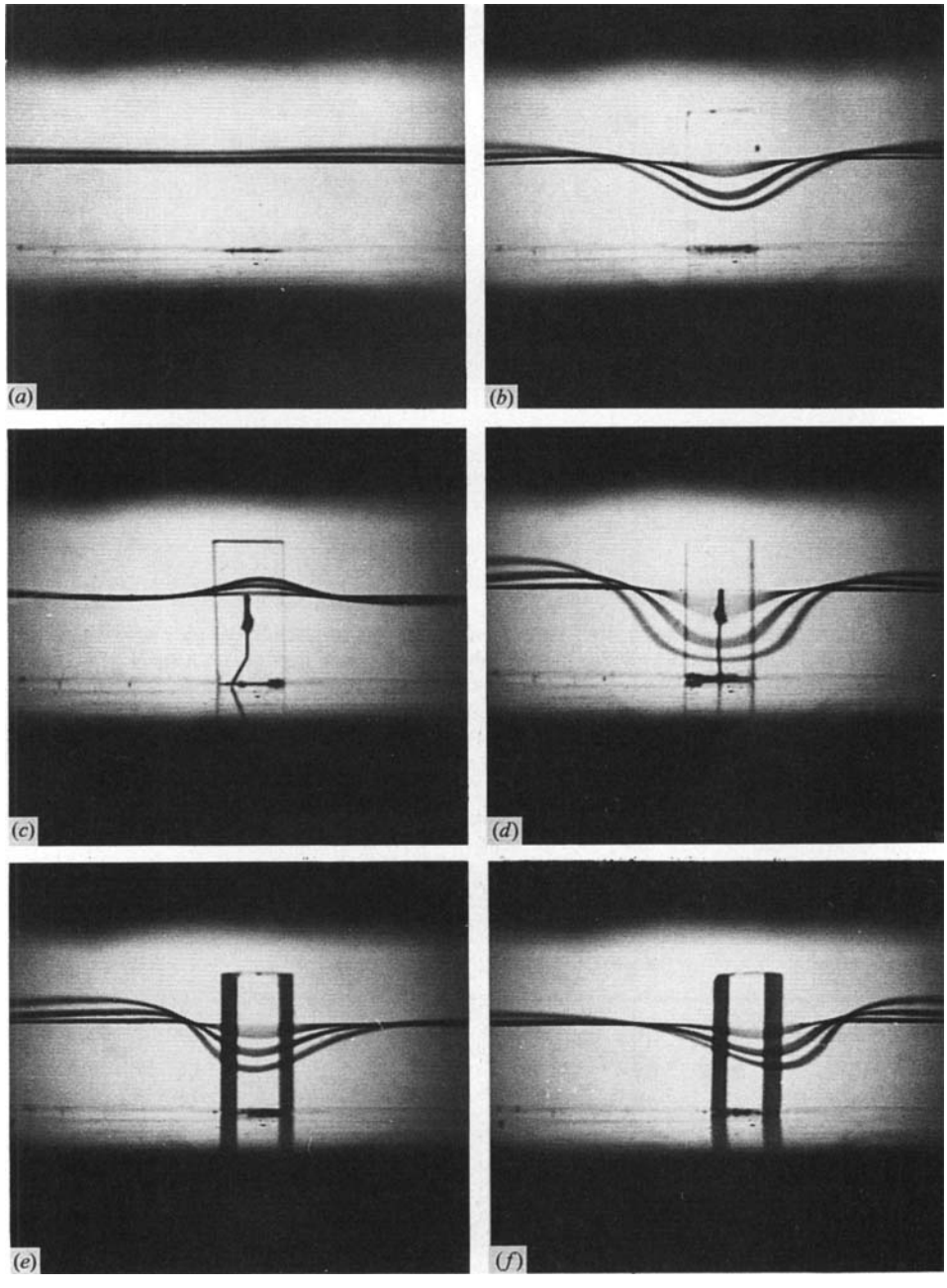

FIGURE 25. As in figure 24, but for a series of tall narrow obstacles, apart from (*a*), which shows the undistorted dye line in the absence of an obstacle; (*b*) the 1×2 rectangle (v); (*c*) the backwards-leaning rectangle (vii); (*d*) the forwards-leaning rectangle (viii); and (*e*), (*f*) plate (v) turned about its vertical axis of symmetry through $+45°$ and $-45°$ respectively.

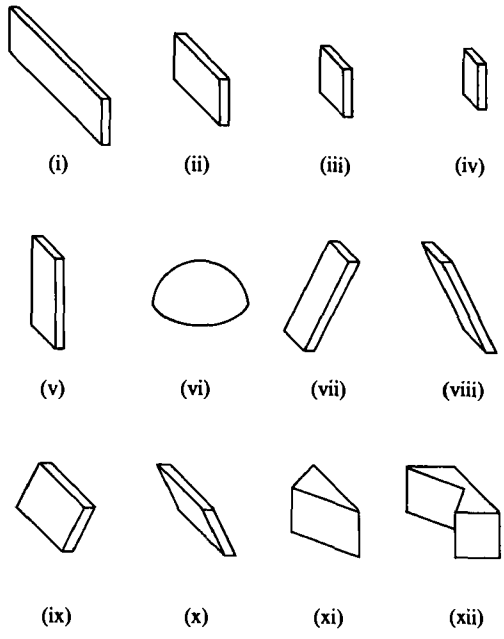

FIGURE 26. The obstacles used in the channel experiments: objects (i)–(iv) are vertical rectangular plates 50, 24, 12.5 and 6.25 mm wide respectively, and 12.5 mm high; (v) is a vertical plate 12.5 mm wide and 25 mm high; (vii) and (viii) are plates tilted 30° from the vertical, back from and forwards into the stream respectively, which extend to 25 mm above the surface and are 12.5 mm wide; (vi) is a hemisphere of radius 12.5 mm; (ix) and (x) also consist of plates tilted 30° from the vertical back from and forward into the stream respectively, these objects extend to 12.5 mm above the surface and are 25 mm wide; and (xi) is a 12.5 mm high prism with horizontal isosceles right triangular section and (xii) is the block from which it was cut. Each object was mounted as illustrated with channel flow from left to right.

Obstacle	h/b	h/δ	$(w/U)\times 10^2$	Obstacle	h/b	h/δ	$(w/U)\times 10^2$
(i)	0.25	1.7	+3.5	(vii)	2.0	1.7	+3.5
		0.8	+2.5			0.8	+5
(ii)	0.5	1.7	+2.5	(viii)	2.0	1.7	−6
		0.8	+2			0.8	−5
(iii)	1.0	1.7	−1	(ix)	0.5	1.7	+3
		0.8	+1			0.8	+3
(iv)	2.0	1.7	−1	(x)	0.5	1.7	−4
		0.8	+1			0.8	−1.5
(v)	2.0	1.7	−3.5	(xi)	0.5	1.7	−4
		0.8	−0.5			0.8	−2
(vi)	0.5	1.7	−2.5	(xii)	0.5	1.7	+4
		0.8	+1			0.8	+3.5

TABLE 2. Representative vertical velocities w at a distance 75 mm downstream from symmetrical obstacles of height h and breadth b in a boundary layer of 2 different depths δ and stream of velocity U

symmetry and varies in magnitude relatively slowly over heights comparable with that of the obstacle. The procedure adopted was therefore to observe dye lines at a distance above the base plane equal in each case to half the height of the obstacle, and to measure transit times and displacements over the range 60–90 mm downstream of the obstacle. The velocities so measured were close to the maximum vertical velocities and were reproducible to within $\pm 0.005U$ for typical values of about $0.03U$, an accuracy about that anticipated and sufficient here. The observations are described below for each of the twelve obstacles illustrated in figure 26, in each case for the two boundary thicknesses $\delta = 7.4$ and 15 mm respectively. The rectangular plates were each of 3 mm thick Perspex sheet.

(i) A 4×1 rectangular plate, 12.5 mm high and 50 mm wide, mounted perpendicular to the base plate and normal to the stream, generates a dominant trailing-vortex pair with upwash on the downstream symmetry plane in the 'thin' (7.4 mm) boundary layer and a slightly weaker vortex pair with upwash in the 'thick' (15 mm) boundary layer.

(ii) A 2×1 rectangular plate, 12.5 mm high and 25 mm wide, vertical and normal to the stream, generates trailing-vortex pairs with upwash similar in each case to the corresponding pair in (i) but a little weaker. This case is shown in figure 24 (*b*), where three successive dye lines may be seen: the most recent is very close to the generating wire and little distorted, the intermediate one largely obscured, and the oldest shows central upwash and downwash to either side of the obstacle corresponding with the dominant trailing-vortex pair.

In each of those two cases with upwash in the wake there is strong upstream separation and flow visualization using dye upstream of the obstacle shows the classic features of the 'horseshoe vortex'. Dye released behind the upstream separation point can be seen to spiral into a vortex core which curves away downstream round the sides of the obstacle, suggesting a downwash vortex pair to the sides of the wake behind the obstacle. However, the dye filaments released from the transverse wire behind the obstacle show no sign of this outer vortex pair. Careful observation of the dye core as it curves round the obstacle shows that its rotation decays very rapidly past the obstacle, and that even where spirals persist there is negligible associated rotation downstream. We are faced with one of the classic problems of attempting to visualize vortices: The diffusivity ν for vorticity is two to three orders of magnitude larger than the diffusivities of many of the markers used to visualize flow, and the vorticity may annihilate by cross-diffusion or merely spread through a large volume in a time in which the dye used suffers little diffusion. The dye, in any case, reflects the motion of the fluid, and it may convey little information about vorticity. In these cases, as we have already seen from the numerical simulation, opposing vorticity is generated at the boundary upstream of the obstacle and is advected upwards and cross-diffuses into the surviving boundary-layer vorticity, progressively annihilating it.

(iii) A 1×1 square plate, 12.5 mm high and wide, produces a weak *downwash* vortex pair in the 'thin' boundary layer, but a weak *upwash* vortex pair in the 'thick' boundary layer. We note that the *square* plate appears to be critical in the sense that it produces upwash vortices where the ratio of obstacle height to boundary-layer thickness is 0.8, and downwash vortices for ratio 1.7.

(iv) A 1×2 rectangular plate, 12.5 mm high and 6.25 mm wide, produces weak downwash vortices in the 'thin' boundary layer and weak upwash vortices in the 'thick' boundary layer, as in case (iii).

(v) A 1×2 rectangular plate, 25 mm high and 12.5 mm wide, produces a strong

downwash vortex pair in the 'thin' boundary layer, illustrated in figure 25(*b*), and a very weak downwash pair in the 'thick' boundary layer. Note that plate (v) has the same aspect ratio as plate (iv), but twice the linear dimensions: thus the Reynolds number $\bar{u}h/\nu$ has more than doubled, and the ratios of body height to boundary-layer thickness have doubled from 1.7 and 0.8 to 3.4 and 1.7 respectively. A comparison of plate (iv) in the 'thin' boundary layer with plate (v) in the 'thick' boundary layer shows that both produce weak downwash vortices, the latter at higher Reynolds numbers being apparently weaker, though the difference lies at the bounds of experimental error.

Two important features emerge from the observations on bodies (i)–(v): (I) *downwash vortices are associated with thin boundary layers and tall obstacles*; and (II) *upwash vortices are associated with low obstacles and thick boundary layers.* The obstacle used in case C of the numerical study just falls into the former category whilst that used in cases A and B is in the latter category. Case C with an object whose height is roughly equal to its width is not a clear cut example of the former category.

(vi) A hemisphere of radius 12.5 mm, produces downwash vortices in a thin boundary layer and upwash vortices in a thick boundary layer. It is impossible at this stage to clarify a hemisphere in terms of shape with the rectangular plates, although we may note that its behaviour is similar to the square plate except that the hemisphere produces rather stronger downwash vortices in a thin boundary layer.

The next set of obstacles consist of rectangular plates which slope either back from or forward into the flow, in each case at 30° inclination to the vertical, but retain the same vertical streamwise plane of symmetry with upper and lower edges normal to the undisturbed stream.

(vii) A rectangular plate, 12.5 mm wide, inclined to the vertical at 30° leaning back from the stream about a lower edge that remains normal to the stream. The top of the plate extends to a height of 25 mm vertically above the floor. In this case much of the oncoming stream is lifted over the crest. There must be changes in the surface pressure field and hence the rate of generation and orientation of vorticity at the surface, and also of velocity gradient around the sides and hence of inertial turning of advected vorticity. These are complex changes but their aggregate effect is to produce trailing-vortex pairs with upwash which are relatively strong for the 'thin' boundary layer and very strong for the 'thick' layer. The former case is illustrated in figure 25(*c*).

(viii) A rectangular plate, 12.5 mm wide inclined forwards into the stream at 30° to the vertical. The top of the plate again extends to a height of 25 mm above the floor. The oncoming stream is here driven downwards and out around the base of the plate, with little flow over the crest and again with corresponding changes both in the direction of pressure-generated vorticity and of its turning with advection in the stream. The result is to produce a dominant trailing-vortex pair with downwash that is extremely strong in the 'thin' boundary layer, illustrated in figure 25(*d*), and very strong in the 'thick' boundary layer.

The effect of body slope away from and into the incident stream is confirmed with the low 2×1 rectangular plate (obstacles (ix) and (x)), which again shows that cross-stream symmetrical bodies with inclined surfaces produce strong trailing-vortex pairs with upwash sense when the flow is defected up and over the obstacle and downwash sense when it is driven down and round the lower corners of the obstacle.

It is clear from the channel experiments that trailing-vortex pairs are a normal feature of the wakes of symmetrical obstacles mounted on a boundary. Moreover, the observations suggest a very simple empirical rule for predicting both the sense

of the dominant trailing-vortex pair and its magnitude: *flows past obstacles that give a flow maximum over their crests produce upwash vortex pairs; and flows past obstacles that give flow maxima to the sides of the obstacle produce downwash vortex pairs.* The strength of the vortex pairs relates to the degree of this diversion of flow by the obstacles. The diversion arises from the combined effect of the shape of the obstacle and the upwind shear. The shear tends to promote a flow maximum over the crest but is easily outweighed by the obstacle shape.

Finally, these empirical laws were tested further with two three-dimensional obstacles consisting of a right prism cut from a rectangular block of height 12.5 mm, width 25 mm and length in excess of 12.5 mm, and the re-entrant remainder of the block from which the prism had been cut.

(xi) A prism, with height 12.5 mm, triangular faces horizontal, placed symmetrically with the right-angled vertex facing into the stream, produces trailing-vortex pairs with downwash. Prisms divide the flow laterally, but they also direct it downwards within the boundary layer to a degree depending on the ratio of body height to boundary-layer thickness. The pressure gradients on the slant faces of the prism directed into the flow act down and out, and the flow is driven round the corners between the base plate and rear edge of the prism. The strong downwash vortices for the 'thin' boundary layer are illustrated in figure 24(*c*); those for the 'thick' boundary layer are relatively weaker (table 2) because the prism is no longer tall relative to the boundary-layer thickness.

(xii) The block from which the prism was cut, when placed symmetrically with the cavity facing upstream produces a strong trailing-vortex pair with upwash, illustrated for the 'thin' boundary layer in figure 24(*d*). In this case there is little dependence on boundary-layer thickness (except that the edge of the 'thick' boundary layer passes above the block) since the oncoming flow is caught in the cavity and forced over the top of the block regardless of its flow profile.

In each of the above cases the flow structure in the neighbourhood of the rear saddle point of the surface stress field was examined by introducing dye onto the surface. All cases with upwash vortices are associated with flow separation (as in case B of the numerical simulation); and those with downwash vortices are associated with flow attachment (as in case C of the numerical simulation).

4.2. *Vortex wakes of asymmetric obstacles*

Vortex wakes of asymmetric obstacles were observed using the 2×1 and 1×2 rectangular plates (ii) and (v) respectively, turned skew to the stream about the vertical axis of symmetry for a range of inclinations of plate face to incident stream and set in the 'thin' boundary layer. As with the symmetric obstacles, wake flow was characterized by photographing distorted dye lines from downstream and by measuring the vertical component of disturbance velocity about 75 mm downstream of the object in the streamwise plane through the rotation axis of the object and at mid-object height. The observed disturbance velocities are given in table 3 for various plate inclinations. For both small incidence ($\approx 0°$) and near normal incidence ($\approx 90°$) of either plate to the stream, the trailing-vortex pairs of a symmetrical obstacle were observed; but for angles of incidence between about 20° and 80° a single trailing vortex dominated the wake. The measurements of vertical velocity in table 3 show that those trailing vortices are strongest around inclination 45°, and illustrations of dye-line distortion are given for plate (ii) in figures 24(*e*, *f*), and for plate (v) in figures 25(*e*,*f*), in each case for plate inclinations to the stream of $+45°$ and $-45°$ respectively. The vertical velocities observed at normal incidence (90°) are those

	θ...	0°	10°	22°	45°	67°	90°
	Obstacle						
$(w/U) \times 10^2$	(ii)	−1	+2.5	+5	+5	+3	+2.5
	(v)	−1	+1.5	+3	+5	+4	−3.5

TABLE 3. Representative vertical velocities w at a distance 75 mm downstream of skew rectangular plates standing in a boundary layer of thickness $\delta = 7.4$ mm and outer stream of velocity $U = 4$ mm s^{-1} for various angles of incidence θ of plate surface to incident stream. Note: at 0° the plate is aligned with, and at 90° normal to the stream

Re ...		17	33	50
	Obstacle			
$(w/U) \times 10^2$	(ii)	+1	+2	+6
	(xi)	−1	−2	−5
	(ii) at 45° inclination	+2	+2	+4

TABLE 4. The effect of Reynolds number, $Re = \bar{u}h/\nu$, on the representative vertical velocity w at distance 75 mm downstream from obstacles standing in a boundary layer of thickness $\delta = 7.4$ mm and outer stream of velocity $U = 4$ mm s^{-1}

appearing in table 2 for symmetrical vertical plates which produce vortex pairs with upwash and downwash for plates (ii) and (v) respectively; and those for zero incidence (0°) correspond with very tall narrow symmetrical obstacles which produce relatively weak vortex pairs with downwash. Note that the general magnitudes of both solitary and pair vortices are broadly similar.

4.3. *Variations with Reynolds number*

At low Reynolds numbers the numerical simulation showed an absence of significant trailing vortices. The flow was dominated by diffusion with corresponding annihilation of vorticity within the general zero circulation in transverse sections downstream of symmetric obstacles. At higher Reynolds numbers than those reported in §3, the flows were too unsteady to handle within the scope of this study.

A limited series of observations was carried out in the channel for two obstacles over the range of Reynolds number extending from just above that required for flow separation at the obstacle to that for marginally unsteady flow. The Reynolds number was varied by changing channel speed, but each obstacle was sited so that the local boundary-layer thickness was constant, $\delta = 10$ mm for all cases. The disturbance vertical velocities for three different situations at three different Reynolds numbers are given in table 4: the situations comprising the 2×1 rectangular plate normal to the stream (ii), the symmetrical prism (xi), and the 2×1 plate inclined at 45° to the stream. At the largest Reynolds number the flow is slightly unsteady and the disturbance velocities are averaged over ten realizations; the accuracy appeared to be similar to that for steady flows. Reynolds-number dependence for the two symmetrical obstacles is large, but changes only the magnitude and not the sense of the trailing-vortex pair, and this is due to the changing role of diffusive annihilation with changing Reynolds number. There is less Reynolds-number dependence in the single trailing vortex behind the asymmetric obstacle, and this is consistent with the

reduced possibilities for short-range cross-diffusive annihilation with the single vortex. In all cases the velocities close to the object were found to be less dependent on Reynolds number than those further downstream, which highlights the very important role of diffusion in annihilation.

5. Summary and conclusions

Flow past surface-mounted obstacles has been examined by means of numerical simulation and laboratory channel-flow experiments. Attention has been confined to Reynolds numbers ≈ 100 and only slightly smaller than the values giving unsteady flow. These are smaller values of Reynolds number than those considered in most previous work on separated flows. The numerical solutions allow a few flows to be examined in detail whilst the laboratory experiments consider a wider range of object shapes.

Diagnostic calculations based on the numerical solutions allow an examination of the mechanisms leading to the production of trailing vortices. In accord with the discussion of basic ideas in §2 it is clear that upstream of the body the adverse pressure gradient produced by the body generates vorticity opposite in sign to the basic boundary-layer vorticity. Upstream of the body and to the sides of the streamwise plane through the centre of the body this pressure field also generates a vortex pair of a sense giving upwash on the centreplane. Before this freshly generated vorticity can diffuse with and annihilate the boundary-layer vorticity both senses of vorticity are subject to inertial turning and stretching. This leads to trailing circulations of both signs but, at the Reynolds numbers considered here, these circulations suffer rapid diffusive cancelling and behind the body they do not persist to a significant degree. In the region around the body the incident boundary-layer vorticity is turned so as to produce a trailing-vortex pair with downwash in the plane of symmetry. This short-lived feature, which corresponds to the 'horseshoe vortex' conceptual mechanism, is significant in flow immediately around the tall body considered – case C. This significance is not due to any dominance of the circulations to either side of the body but a consequence of the local concentration of vorticity. In flows at higher Reynolds number previous work suggests that this feature is more pronounced. In the region downstream of the body there will be surviving trailing vorticity from this upstream generation and turning, but fresh sources will also arise.

As the flow is driven by pressure gradients over and around the body, predominantly transverse vorticity is generated by the pressure gradient at the surface of the body. The vorticity generated over the body then leaves the surface and becomes the boundary of the wake. Although this generation gives some streamwise vorticity and associated slope or orientation of the separation lines we have not found this a particularly significant effect. The inertial processing which is not independent of this generation but which occurs after flow separation seems more important. Apart from residues of vorticity from upstream, just downstream of the obstacle the simulations show three noteworthy causes of trailing circulations. These are (*a*) the inertial processing of the transverse velocity shear comprising the boundary of the wake, (*b*) the inertial turning of transverse boundary-layer vorticity to the side of the wake, and (*c*) pressure generation at the surface. Owing to the low pressure just behind the body the pressure generation gives a vortex pair with downwash. The turning of vorticity to the side of the wake is dominated by the decrease in flow speed away from the maximum to the side of the wake and is of a sense to give a vortex pair with upwash. The sense of the turning of vorticity in the

shear layer is harder to decide. Indeed the sign seems to depend on both the body shape and the influence of upwind shear. These generation mechanisms add to the circulations remaining from those generated upstream. We can offer no compelling argument to say which of the various contributions should dominate net circulations to either side of the body. An important feature of all the transverse sections of the flows past objects with cross-stream symmetry is the small magnitude and unimportance of the net circulations in the quadrants to either side of the body. In general the individual areas of a single sign of vorticity have circulations at least an order of magnitude greater than the net values. The numerical results suggest that the turning of vorticity in the shear layer is most significant in giving dominant regions of *concentrated* vorticity. This is perhaps a natural consequence of the turning of the most concentrated lateral components of vorticity. The sense of the inertial turning in the shear layer depends upon the flow structure arising from the upwind shear and the body shape. In the numerical examples, the squat body (case B) generates a vortex pair with upwash on the plane of symmetry whilst the tall bluff body (case B) produces one with downwash on the plane of symmetry. Vortex pairs of such senses dominate the wakes of these examples.

As the trailing vortices proceed downstream they suffer mutual annihilation and their strengths decline. However mutual interactions and inertial processing allow the features to remain concentrated. In the present study it is evident that the trailing circulations modify the streamwise flow. At the Reynolds numbers we have considered this process is not very rapid and only at the exit of the numerical domain is it important. At this stage it seems that the pattern of vorticity generation is modified. We speculate that at higher Reynolds number a more complex interaction of vortices with the basic boundary layer will occur.

In the example of flow past a body mounted skew to the stream the only real change was a lack of cross-stream symmetry. In consequence of such asymmetry the wake downstream of the body was dominated by a single concentrated vortex. Although the sense of this vortex corresponds to that expected if the obstacle were viewed as one half of a lifting body, the simulations confirmed the difference anticipated in §2. In the computational domain the net trailing circulation was more than an order of magnitude less than the circulation in the concentrated single vortex. But for the finite separation of the lateral boundaries the net circulation would have been zero. To the side of the concentrated vortex there is a broad distribution of vorticity of the opposite sign.

The laboratory observations with a wide range of object shapes and boundary-layer depths enable us to suggest some empirical rules for determining the dominant sense of trailing-vortex generation. A vortex pair with central upwash is promoted by deep boundary layers and objects that are wide in relation to their heights. A vortex pair with central downwash is promoted by a thin boundary layer and objects that are tall in relation to their heights. The inclination and detailed shape is also found to be important. A single empirical rule that matches all observations of objects with cross-stream symmetry emerges: obstacles with a distinct flow maximum over their crests produce upwash vortex pairs whilst those that divide the flow laterally and are able to give flow maxima to their sides give downwash pairs. Although the shape of an obstacle plays the dominant role when the ratio of the height to breadth is not near unity, upwind shear may determine the nature of flow past obstacles with height/breadth ratios near one. This rule is consistent with the suggestion that the inertial turning of the lateral vorticity comprising the boundary of the wake is of particular importance.

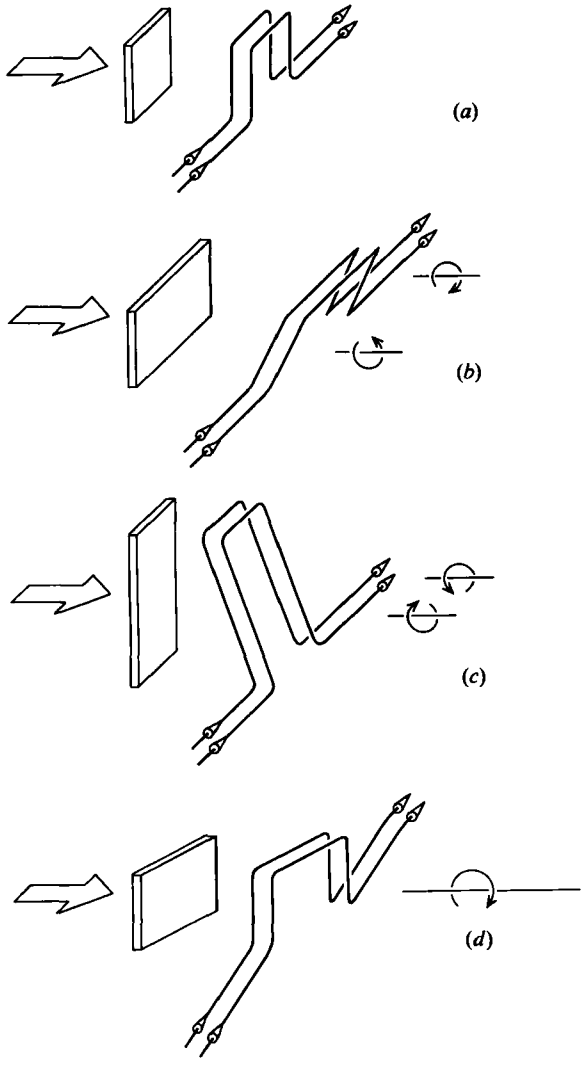

FIGURE 27. Schematic illustration of the *dominant* sense of tilting and twisting of vortex filaments in the wake of obstacles. The sense of the corresponding dominant trailing-vortex circulations are indicated. Note that although this illustration indicates the gross features of the vortex filament connectivity it ignores both the initial and developing complexities of the structure. Case (*a*) shows a 'neutral' body with no trailing vortices, (*b*) a squat body with a flow maximum over the crest and upwash vortices, (*c*) a tall body with a flow maximum to the sides and downwash vortices, and (*d*) a skew body with a dominant single vortex.

Finally it is useful to consider the connectivity of the vortex filaments in flow past surface-mounted obstacles. This connectivity is implicit in the discussion of basic ideas given in §2. Viewed in its broadest terms the presence of an arbitrary obstacle only generates filaments in closed loops. The whole flow can be considered as an addition of various closed loops to the undisturbed boundary-layer vorticity. The latter is viewed locally as transverse filaments of supposed infinite extent. When the locally generated loops are oriented in vertical planes they have no component in the streamwise direction and can only describe the basic structure of flow reductions and accelerations around the obstacle. The trailing vortices arise as the loops are

distorted out of vertical planes either with cross-stream symmetry for cross-stream symmetric bodies or with no such symmetry for skew bodies. It is clear from the complex patterns of streamwise vorticity that it would be very difficult to illustrate the vortex connectivity of any real flow that we have considered. At considerable risk of oversimplification we have provided a schematic illustration (figure 27) of the local vortex-filament distortions implied by the *dominant* trailing circulations that we have observed. This illustration of the dominant vortex structure in the wake neglects both initial details and the inevitable tendency for distortions to be self-induced as the structure propagates downstream. Figure 27(*a*) shows a local section of vortex filaments behind a body with no trailing circulation. The addition of vertical loops to the boundary-layer filaments gives a loop structure which describes the wake. Figures 27(*b*, *c*) show how upwash and downwash vortex pairs imply a tilting to and fro of the top of the loop relative to body. In figure 27(*b*) a squat body has a flow maximum over its crest and this tilts the loop so that the top of the loop extends downstream, whilst in figure 27(*c*) a tall body has a flow maximum to the sides and the top of the loop trails behind. Figure 27(*d*) illustrates a skew loop structure consistent with a dominant single trailing vortex. Allowance has been made for a wider distribution of opposite vorticity to the sides of the body.

We do not speculate in any detail upon the generation of trailing vorticity in unsteady and turbulent flows at high Reynolds number. There can be little doubt that many of the ideas revealed here will have some application but a number of new effects will no doubt be important.

REFERENCES

Baker, C. J. 1979 The laminar horseshoe vortex. *J. Fluid Mech.* **95**, 347–367.

Baker, C. J. 1980 The turbulent horseshoe vortex. *J. Wind Engng Indust. Aero.* **6**, 9–29.

Cook, N. J., Coulson, B. H. & McKay, W. 1978 Wind conditions around the Rock of Gibraltar. *J. Indust. Aerodyn.* **2**, 289–309.

Gregory, N. & Walker, W. S. 1956 The effect of transition of isolated surface excrescences in the boundary layer. *Aero. Res. Counc. R & M* 2779, Pt 1.

Hansen, C. A. 1975 Vortex-containing wakes of surface obstacles. Dissertation, Colorado State University, Fort Collins, Colorado.

Hunt, J. C. R. 1971 The effect of single buildings and structures. *Phil. Trans. R. Soc. Lond.* A **269**, 457–467.

Hunt, J. C. R., Abell, C. J., Peterka, J. A. & Woo, H. 1978 Kinematical studies of the flow around free or surface mounted obstacles; applying topology to flow visualization. *J. Fluid Mech.* **86**, 179–200.

Hunt, J. C. R. & Snyder, W. H. 1980 Experiments on stably and neutrally stratified flow over a model three-dimensional hill. *J. Fluid Mech.* **96**, 671–704.

Jenkins, G. J., Mason, P. J., Moores, W. H. & Sykes, R. I. 1981 Measurements of the flow structure around Ailsa Craig, a steep, three-dimensional isolated hill. *Q. J. R. Met. Soc.* **107**, 833–851.

Lighthill, M. J. 1963 In *Laminar Boundary Layers* (ed. L. Rosenhead), pp. 48–113. Oxford University Press.

Mason, P. J. & Sykes, R. I. 1979*a* Three-dimensional numerical integrations of the Navier–Stokes equations for flow over surface mounted obstacles. *J. Fluid Mech.* **91**, 433–450.

Mason P. J. & Sykes, R. I. 1979 *b* Separation effects in Ekman layer flow over ridges. *Q. J. R. Met. Soc.* **105**, 129–146

Mason P. J. & Sykes, R. I. 1981 A numerical study of rapidly rotating flow over surface mounted obstacles. *J. Fluid Mech.* **111**, 175–195

MOCHIZUKI, M. 1961 Smoke observation on boundary layer transition caused by a spherical roughness element. *J. Phys. Soc. Japan* **16**, 995–1008.

MORKOVIN, M. V. 1972 An approach to flow engineering via functional flow modules. *Beitrage zur Strommungslehre, Insbesondere Grenzschicht Theorie, Deutsche Luft and Roumfahrt, Forschungsbericht*, 72–27.

MORTON, B. R. 1984 The generation and decay of vorticity. *Geophys. Astrophys. Fluid Dyn.* **28**, 277–293.

PIACSEK, S. A. & WILLIAMS, G. P. 1970 Conservation properties of convection difference schemes *J. Comp. Phys.* **6**, 392–405.

SEDNEY, R. 1973 A survey of the effects of small proturberances on boundary layer flows. *AIAA J.* **11**, 782–792.